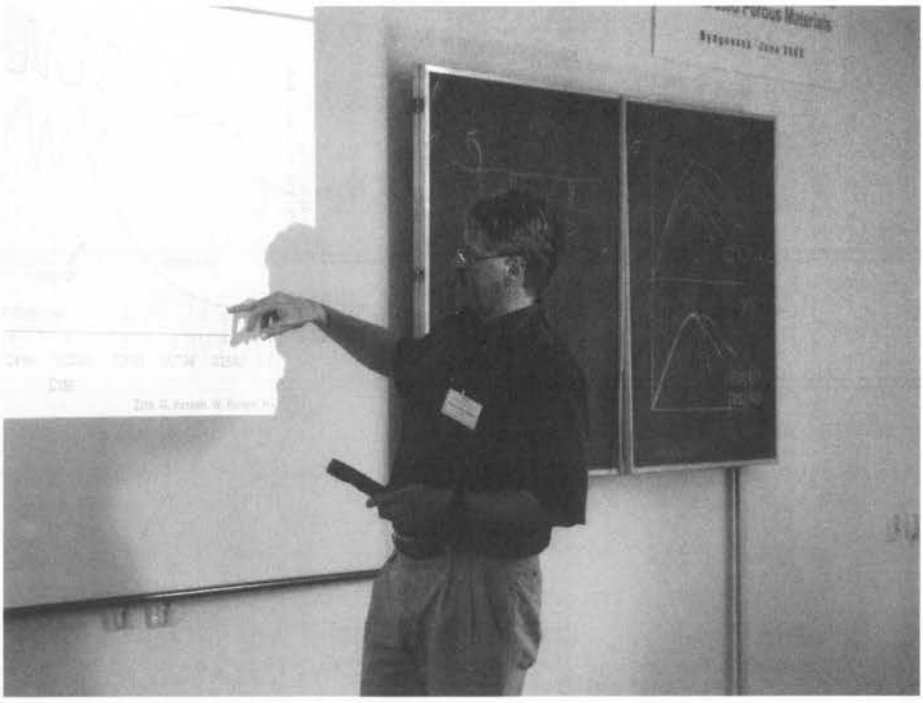

MODELLING COUPLED PHENOMENA IN SATURATED POROUS MATERIALS
POROCENT - (PP.351–416) - BYDGOSZCZ, JUNE 2003.

Coupled mechanical phenomena in deformable porous media

H.-J. Kümpel

Leibniz Institute for Applied Geosciences, Geozentrum Hannover
Stilleweg 2, D-30655 Hannover, Germany
kuempel@gga-hannover.de

In porous, fluid saturated media, changes in pore pressure and matrix strain are inevitably related to each other. Numerous field observations have revealed that linear poroelasticity may often be applied to phenomena occurring in fluid saturated, geological formations. Application of the concept of Biot's theory of consolidation in such cases requires knowledge of the relevant poroelastic parameters and the values they take for real rock material. The present notes address coupled mechanical phenomena in saturated porous rocks from elementary considerations on petrophysical parameters to solutions of numerical modelling. Examples of field cases show where coupled deformation is crucial for the understanding of the physical processes that are involved.

Key words: *poroelasticity, effective medium parameters, Biot's theory, well-aquifer systems*

1. Introduction

1.1. Strange well level changes

A surprising observation to the non-expert is that pore pressure in the vicinity of a pumped well can rise whereas a drop of pore pressure is expected. Fig. 1 shows well level recordings of such a case. Changes in pore pressure, here, are reflected in the response of water levels in wells that are hydraulically connected to some aquifer - actually two distinct aquifers at this particular site. The phenomenon of inverse pore pressure response is occasionally reported in the literature. It is often called 'Noordbergum effect', referencing the name of a Dutch village in the vicinity of which the effect was also observed [2, 3].

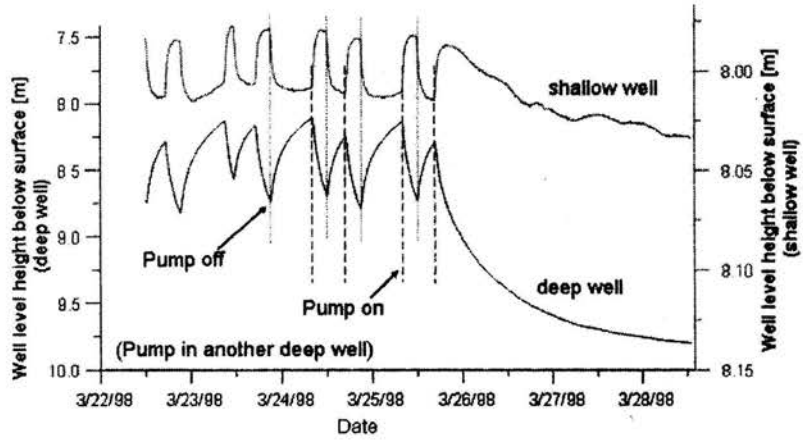

Figure 1: Rising or falling well water level in a shallow well (upper curve) when pumping is initiated or stopped in a deeper aquifer, respectively. Observation shown was made near Holßel, a village in Northern Germany (data from [1]). Unlike in the shallow well, variation of well water level in a deep well (lower curve) placed adjacent to the pumped well is as expected. For a longer phase of pumping, the well level after initial rising also drops in the shallow well (visible on the right). Note different scales for the two well level curves.

Occurrence of the Noordbergum effect gives evidence that classical elasticity fails to explain certain deformation processes in saturated porous media. The effect is in fact a 'beautiful' example for the strong coupling between pore pressure and deformation of the rock matrix. Understanding of the phenomenon requires insight into poroelastic rheology. As will be seen later, elasticity is still the basis but not sufficient to explain the Noordbergum effect.

1.2. Rheological concepts

Rheology describes the way a medium reacts to mechanical forces. The most commonly known and most widely applied rheological concept is linear elasticity as described by Hooke's law, or as imaged by a spring element: Deformation of elastic media is exactly proportional to the applied forces, and is fully reversible. Other well known rheologies are e.g. viscosity according to Newtonian fluid flow and plasticity, also called Saint Venant rheology.

In this article, parameters describing the well known behaviour of an elastic medium if submitted to forces are listed in Table 1. To emphasize that

Young's modulus	E'	$= 3(1-2\nu')K'$
Bulk modulus	K'	$= \ldots$
Compressibility	c'	$1/K'$
Shear modulus Modulus of rigidity	μ' G'	$= 0.5\ E'(1+\nu')$
Poisson's ratio	ν'	$0 \geq \nu' \geq 0.5$
2 nd Lamé parameter	λ'	$= \ldots$

Table 1: Most frequently used elastic parameters with some interrelations. Two of the parameters suffice to characterise elastic behaviour of a homogeneous, isotropic medium. Strings are used to highlight that the parameters hold for compact, non-porous materials.

elastic material is compact rather than porous, we use strings with notations of elasticity parameters. Some classical lay outs of laboratory tests to quantify the respective parameters are shown in Fig. 2. In case of a fluid saturated medium, a compression test to establish the value of the bulk modulus of a sample can be conducted in at least two different ways: the sample can either be allowed to drain i.e., to loose some portion of its pore fluid - or not (see Fig. 3). Depending on the conditions of drainage, the sample's volume reduction in response to an increase in confining pressure, noted as P_c, will be

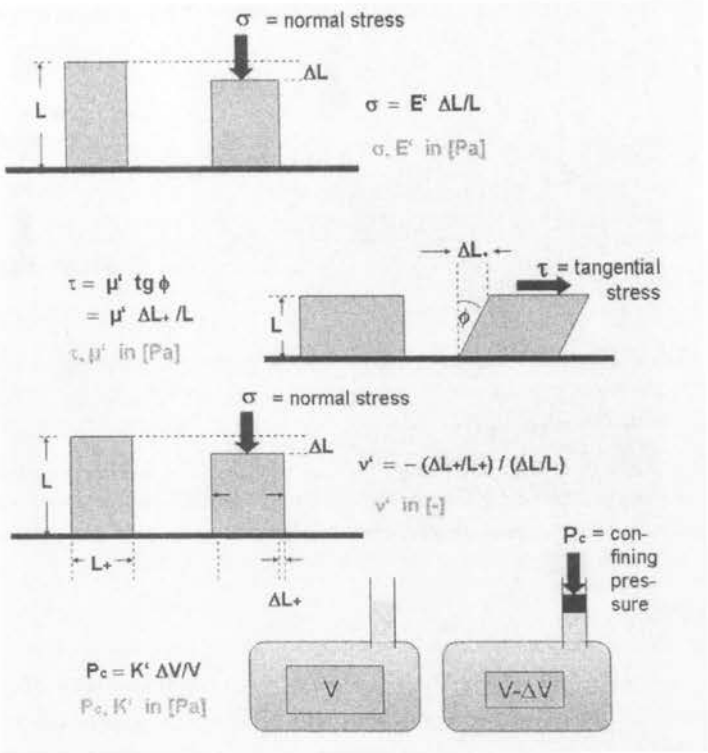

Figure 2: Sketch of tests to establish values of four different types of elastic parameters: Young's modulus E', shear modulus μ', Poisson's ratio ν', and bulk modulus K' (from top to bottom). Note the differences in the type of applied forces i.e., normal stress σ, tangential stress τ, and confining pressure P_c. Friction at the base of the sample is assumed to be zero in tests where normal stress is applied.

different: It will be stronger in case of drainage, and will be less if drainage is prohibited. Accordingly, at least two types of bulk moduli need to be considered: K for the drained case and K_u for the undrained case.

As all natural rocks have non-zero porosity, we will generally use 'non-stringed' symbols for geological materials. In practice, the behaviour of a rock may, however, not significantly differ from that of a compact elastic medium. Then, use of elastic rock parameters may be justified. In cases where porosity and influence of change in pore fluid pressure in a deformation process is not negligible, we will see that poroelasticity is often the better suited rheology to describe the mechanical behaviour of the medium.

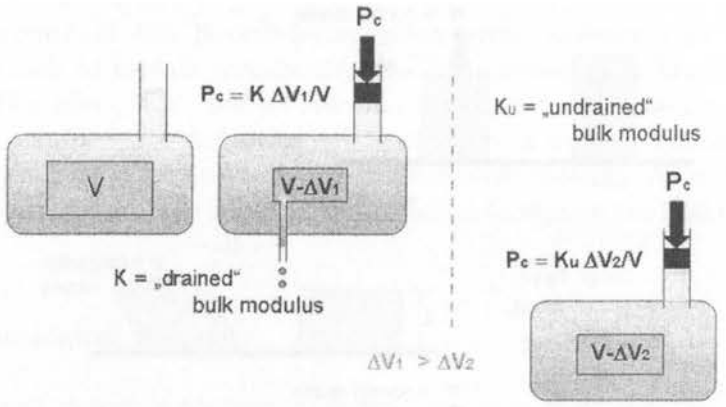

Figure 3: Two different tests to quantify the bulk modulus of a saturated porous medium. Depending on the conditions of drainage, the established bulk modulus holds for either drained or undrained conditions.

1.3. Overview

In the following (section 2), the most useful parameters of poroelastic media will be introduced. As the knowledge of parameter values is indispensable for application of poroelasticity to real problems, typical ranges of such values, for geological material, are given as well. In section 3, the theory of linear poroelasticity will be outlined. It will be shown that a mere combination of Hooke's law of elastic deformation and Darcy's law of fluid flow through a permeable medium forms the basis for poroelasticity - or for three dimensional consolidation as the theory was originally named by Biot in his classical paper [4]. Section 4 has some fundamental solutions that can readily be applied to solve specific problems, or to check numerical results. Finally, a number of case studies on the field scale are presented in section 5. Particular emphasis is laid on illustrations, given here as either figures, tables or plates (displaying mathematical expressions). They facilitate understanding and should also convey that application of the concept of poroelasticity can be fun. Note that this is a brief, in parts simplified treatise of poroelasticity and possible applications. More in-depth presentations can be found in the literature, for instance in [5].

2. Parameters of poroelastic media

2.1. Drained and undrained conditions

Similar as the bulk modulus, other parameters of saturated porous media too hold for either drained or undrained conditions - with one exception: the shear modulus μ. The latter is taken as independent of the conditions of drainage. Although this assumption may be questioned for real rock material, it is substantial in Biot's theory of consolidation. As a consequence, pure shear deformation does not lead to a change in pore pressure and vice versa. Table 2 lists some useful interrelations of poroelastic parameters; Table 3 displays why values of undrained moduli E_u, K_u, λ_u are always equal to or larger than the respective drained moduli E, K, and λ.

2.2. Poroelastic parameters of compressibility

There are basically four parameters that describe how a sample of a poroelastic medium responds to changes in confining pressure. One holds for drained conditions and is named drained or matrix compressibility c. When sufficient time is given, the pore pressure P inside the sample remains unchanged, irrespective of the change in confining pressure P_c (Plate 1, top). When drainage of pore fluid is inhibited, we obtain the compressibility for undrained conditions, or simply undrained compressibility c_u. The situation is characterized by zero mass change whatever the change in P_c would be (δm=0; Plate 1, middle). In both cases it is assumed that the sample is coated by an impermeable skin (of mechanical resistance much less than that of the sample's matrix) so that no mass exchange between the fluid transferring the confining pressure and the pore fluid inside the sample takes place. The tests to establish values of these parameters have already been sketched in Fig. 3.

Although c denotes the compressibility of the matrix, i.e. of solid material, it does not reflect the compressibility of the grains that form the matrix. If

Young's modulus	E E_u	$= 3(1-2\nu)K$ $= 3(1-2\nu_u)K_u$
(also undrained)	ν { $= 0.00$ $= 0.25$ $= 0.50$	$\rightarrow E = 3\,K$ $\rightarrow E = 1.5\,K$ $\rightarrow E = 0$ (liquid!)
Shear modulus	μ $= (!)\ \mu_u$	$= 0.5\,E/(1+\nu) =$ $= 0.5\,E_u/(1+\nu_u)$
$\mu \leq E$ (also undrained)	ν { $= 0.00$ $= 0.25$ $= 0.50$	$\rightarrow \mu = 0.5\,E$ $\rightarrow \mu = 0.4\,E$ $\rightarrow \mu = 0.33\,E$ (liquid!)
2 nd Lamé parameter	λ λ_u	$= 2\mu\nu/(1-2\nu)$ $= 2\mu_u\nu_u/(1-2\nu_u)$
$\mu \leq E$ (also undrained)	ν { $= 0.00$ $= 0.25$ $= 0.50$	$\rightarrow \lambda = 0$ $\rightarrow \lambda = \mu$ $\rightarrow \lambda =$ undetermined (liquid!)

Table 2: Frequently used poroelastic matrix parameters with some interrelations, given for different values of Poisson's ratio ν. The shear modulus μ is independent of the conditions of drainage. $\nu = 0$ and $\nu = 0.5$ are extreme values and hold for media of zero compressibility or incompressible material, respectively. $\nu = 0.5$ also holds for liquids (zero shear resistance).

as $\mu = \mu_u$	E_u	$= E(1+\nu_u)/(1+\nu)$	$\geq E$
	K_u	$= K(1-2\nu)(1+\nu_u)/((1-2\nu_u)(1+\nu))$	$\geq K$
	λ_u	$= \lambda\nu_u(1-2\nu)/(\nu(1-2\nu_u))$	$\geq \lambda$

Table 3: Interrelations of poroelastic matrix parameters for drained and undrained conditions.

the impermeable coating would be missing, an exchange of pore and external fluids will occur, and result in a change in P which - after some time of adjustment - will be equal to the change in P_c (Plate 1, bottom). Then, obviously, only the grains of the matrix will be affected from a change in P_c - rather than the whole porous skeleton. The respective compressibility is called grain or solid material compressibility c_s. (A change in the grain contacts and in the cohesion of the matrix that might have an influence on the volume of the sample would be accounted for by the matrix compressibility c.) The fourth compressibility is that of the fluid phase (the pore fluid) and

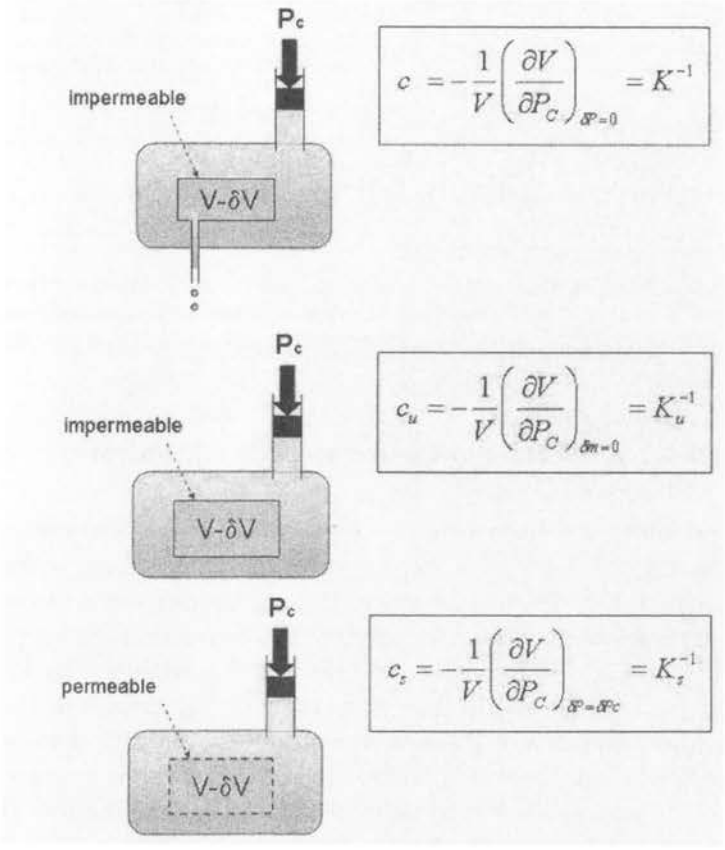

PLATE 1: Three different measures of compressibility for poroelastic media: matrix compressibility c, undrained compressibility c_u, and (solid) grain compressibility c_s with defining expressions, respectively. Bulk moduli are the inverse of the respective compressibilities.

will be noted as c_f here.

Of interest for practical purposes is often the amount of fluid volume that can be stored in a porous medium. In hydrology, it is generally quantified by the storage coefficient. The parameter can also be expressed in units of compressibility. Table 4 has three different definitions of storage parameters. They all hold for one-dimensional consolidation of a porous medium, a simplification which is frequently adopted in hydrology. In 3-D, the storage compressibility S can be shown to equal $c\text{-}c_s + n(c_f\text{-}c_s)$ where n is the volume porosity of the medium (e.g., [6]).

storage coefficient after Theiss	S_T	$[-]$	volume of pore fluid that can be stored in an aquifer per unit area and pore preassure change (as height of water column)
specific storage coefficient	$S^\star$	$[1/m]$	$= S_T/M$ (M= aquifer thickness)
storage compressibility, hydraulic capacity	S	$[1/Pa]$	$= S_T/(M\ g\ \varrho_f)$ as S_T, but with pore pressure change in Pascal; g= gravitational acceleration

Table 4: Various definitions of the 1-D storage parameter for porous media. Frequent use of this quantity is in hydrology or reservoir engineering where it is generally referred to some aquifer or oil formation thickness, M. ρ_f denotes density of the pore fluid.

2.3. Coefficient of effective pressure and Skempton ratio

Two parameters are particularly characteristic for saturated porous media. When the strength of a porous medium is tested, it is found to be proportional to the effective pressure, P_e, i.e. the difference of confining pressure P_c and a fraction of the pore pressure P. The fraction of pore pressure is expressed by a coefficient of effective pressure, α, multiplied by P. To be more exactly, the concept of effective pressure holds for changes in P_e rather than for the absolute value of P_e. α, a dimensionless quantity that can take values between zero and one, is the first of the characteristic parameters in poroelasticity. It can be shown to equal $1\text{-}c_s/c$ [7] and to be less than or equal to porosity n [8]. Accordingly, if matrix compressibility c is not much different from grain compressibility c_s, α is close to zero. Plate 2 has the essential expressions for α and lists typical ranges that values of α take for sediments and rocks.

$$P_e = P_c - \alpha P \quad \text{or} \quad \boxed{\delta P_e = \delta P_c - \alpha\, \delta P}$$

It is $\alpha = 1 - c_s/c \rightarrow 0 < \alpha < 1$ and $n \leq \alpha$

	loose sediments	hard rocks
typical :	$0.7 < \alpha < 1.0$	$0.1 < \alpha < 0.8$

PLATE 2: Definition of the coefficient of effective pressure, α, via the concept of effective pressure P_e and some relations for α.

The other quantity of particular meaning in poroelasticity is the Skempton ratio B (or Skempton coefficient; introduced by Skempton [9]). B denotes the change in pore pressure P per unit change of confining pressure P_c under undrained conditions. Plate 3 shows a test through which B can be measured and has some useful relations. Obviously, B too is dimensionless

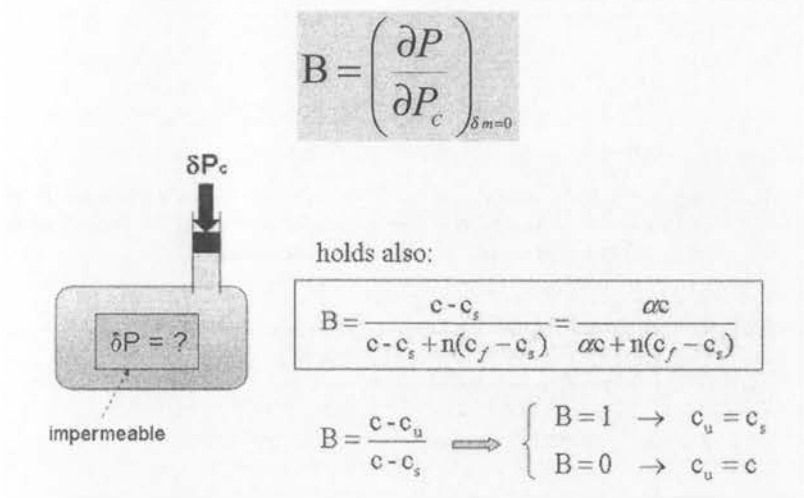

PLATE 3: Definition of the Skempton ratio B and some useful relations with other poroelastic parameters. δm=0 denotes zero mass change i.e., undrained conditions.

and can take values between 0 and 1. When fluid saturation is incomplete B rapidly approaches values close to zero. For 3-D consolidation, the storage and matrix compressibilities are related to the coefficient of effective pressure and the Skempton ratio by $S=\alpha c/B$.

2.4. Quasi-static versus dynamic parameters

Table 5 displays typical ranges of values of poroelastic matrix parameters for loose sediments (sands, clay, mud, silt etc.) and hard rocks (e.g. sandstone, limestone, shists, crystalline rocks). It is noteworthy that the values apply for quasi-static (as opposed to dynamic) forcing that is when terms of inertia can be neglected. The latter is explicitly not the case with the propagation of seismic waves.

As elastic parameters can also be quantified by seismic methods

(cf. Table 6), it may be asked whether dynamic and quasi-static tests reveal identical parameter values. Experimental tests have revealed that this is

	loose sediments	hard rocks
ν	0.1-0.2	0.1-0.35
ν_u	0.3-0.48	0.15-0.4
E	0.2-5 GPa	2-100 GPa
μ	0.1-3 GPa	1-50 GPa
K	0.1-5 GPa	1-100 GPa

K_f ca. 2GPa (Water)

Table 5: Range of values for Poisson's ratios ν, ν_u, drained Young's modulus E, shear modulus μ, and drained bulk modulus K for two categories of rocks, as well as bulk modulus of water, K_f, for surface conditions.

$v_s = \sqrt{\frac{\mu^\star}{\varrho}} \rightarrow$	$\mu^\star(\varrho, v_s)$
$v_p = \sqrt{\frac{K^\star + 4/3\mu^\star}{\varrho}} \rightarrow$	$K^\star(\varrho, \mu^\star, v_p)$
$\Uparrow$	$\mu^\star = \frac{v_p^2 - 2v_s^2}{2(v_p^2 - v_s^2)}$

	loose sediments	hard rocks
$E^\star$, $\mu^\star$	2 - 100 times larger ...	5% - 50% larger ...

... than E, μ

Table 6: Seismic velocities v_s and v_p and their use to deduce elastic parameters $\mu^\star$, $K^\star$, and $\nu^\star$(top). ϱ denotes density. An asterisk is set to signify that the parameters originate from dynamic rather than quasi-static forcing. Factors between quasi-statically and dynamically established values reflect very gross ranges (bottom).

generally not the case [e.g., 10, 11, and 12]. Since the passage of a seismic wave, on one hand, is too fast to allow for pore pressure adjustment inside the pore structure, dynamically obtained values can be taken as estimates of undrained rather than of drained parameter values. On the other hand, if the pore space is filled with (highly compressible) gas, the seismically deduced values will resemble drained parameter values more than undrained ones.

2.5. Hydraulic diffusivity

So far, we have considered poroelastic medium parameters that account for matrix deformation but not for fluid flow within the pore space.

Darcy's law - describing how fluid flow through a rock's matrix depends on permeability, fluid viscosity and pore pressure gradient - provides an easy access to the latter process. As various parameters of fluid flow are in use, it may be helpful to first recall their individual meanings (see Plate 4).

$$q_i = -\kappa \frac{\partial P}{\partial x_i}$$

$q_i =$ volume of pore fluid flowing per unit area and unit time in x_i direction

$\kappa =$ (intrinsic) permeability **k** of matrix per (dynamic) viscosity η of pore fluid

intrinsic permeability	k		[m²]
Darcy velocity	q		[m/s]
Darcy conductivity	κ	= k/η	[m²/Pa s]
hydraulic conductivity	K or Kf -value	= $\kappa \rho f$ g	[m/s]
transmissivity	T	= K M	[m²/s]

PLATE 4: Darcy's law of fluid flow through a permeable matrix (top) and various measures of fluid flow (bottom). ρ_f denotes density of the pore fluid, g is gravitational acceleration, and M is aquifer thickness.

According to Darcy's law, fluid flow can only take place for a non vanishing pore pressure gradient. Yet, a pore pressure gradient in poroelasticity is inevitably coupled to matrix deformation. Hence, fluid flow in a permeable structure is always related to deformation - and vice versa.

Since deformation of a permeable rock that is induced by pore pressure gradients is often not noticeable, it is not always explicitly taken into account in hydrology. However, this can clearly not be accepted in poroelasticity. Therefore, the parameter which describes fluid flow in poroelasticity is one that must intrinsically be related to the elasticity of the matrix. That parameter is called hydraulic diffusivity, D, and is given by the expression noted in Plate 5. D is actually defined by the diffusivity equation for the term $P/B\text{-}P_c$ [13]. It may be interesting to note that permeability k does not occur as an isolated quantity in poroelasticity but exclusively in form of the Darcy conductivity κ (see Plate 4).

$$D = \frac{2}{9}\frac{(1-\nu)(1+\nu_u^2)}{(1-\nu_u)(\nu_u-\nu)}\kappa\mu B^2$$

- unit ? → $[m^2/s]$ as any (!) diffusivity parameter, because D is coefficient in diffusivity equation
- general form → $\frac{\partial\psi}{\partial t} = D\frac{\partial^2\psi}{\partial x_i^2}$ → $[\,./s] = [m^2/s]\,[\,./m^2]$
- here: $\frac{\partial(P/B-P_c)}{\partial t} = D\frac{\partial^2(P/B-P_c)}{\partial x_i^2}$ without deduction

typical	gravel	sand	clay
D $[m^2/s]$	100	1	10^{-6}

PLATE 5: Definition of hydraulic diffusivity D as expression of other petrohydraulic parameters (top), via the diffusion equation (middle) [13], and order of magnitude of values for D (bottom).

In the literature, unfortunately, use of poroelastic parameters and their symbols is all but consistent. This may lead to confusion and even prevent individual researchers from application of poroelasticity. For a review on different notations and definitions of parameters see [6] or [14]. The most complete treatise of poroelasticity can actually be found in [5].

3. Theory of linear poroelasticity

3.1. Introductory considerations

Knowing the relevant parameters describing the behaviour of a poroelastic medium, we may now address the role that forces take in changing the state of stress or pore pressure inside the medium. Plate 6 resumes the types of forces that can act on bodies i.e., on points, surfaces and volumes (whereby point forces are mathematical idealisations that are not met in material physics). Application of poroelasticity, too, assumes various idealisations (see

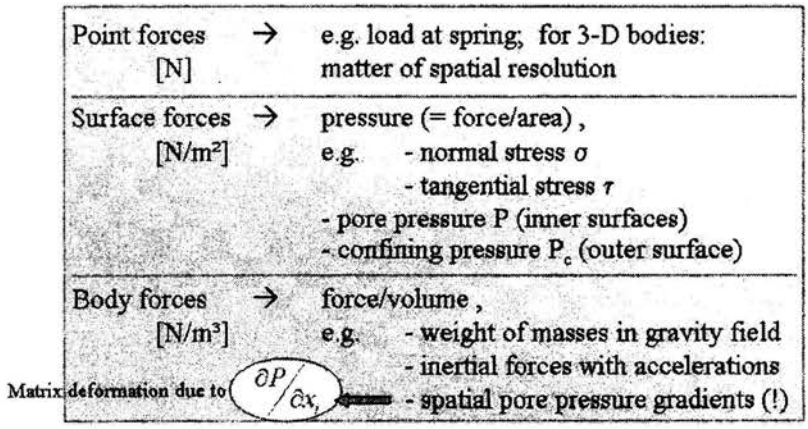

PLATE 6: Mechanical forcing of solid material through point forces, surface forces, and body forces. Pore pressure P acts like a surface force, pore pressure gradients in space $\delta P/\delta x_i$ act as body forces.

Table 7). Most remarkably, it presents a macroscopic continuum approach to processes in a microscopically structured medium. Accordingly, any pore (or cleft) should be much smaller than the considered representative volume. As the theory is a linear one, solutions to individual boundary conditions can be readily stacked to simulate more complex situations. In principle,

medium is continuum	→	no resolution of pore structure
validity of Hooke's law	→	small forces and strain only
validity of Darcy's law	→	laminar flow only
medium parameters are constant	→	independent of pressure and strain
processes are isothermal	→	no changes in temperature
medium is chemically inert	→	constant composition of medium
medium is isotropic	→	same behaviour in all directions
medium is saturated	→	only small amount of pore gas
fluid and skeleton immiscible	→	two 'effective' phases

Table 7: Preconditions for validity of linear poroelasticity and consequences.

the theory of poroelasticity is simply a clever combination of Hooke's linear law in 3-D with Darcy's law of fluid flow in permeable media. The theory is based on the 1-D solutions of Terzaghi [15] and Biot's theory of three dimensional consolidation [4]. The latter has been reformulated by Rice and Cleary [13] with use of parameters which are more easily accessible to laboratory tests than the ones introduced by Biot. For consistence use of notations, Plate 7 recalls Hooke's law for 3-D bodies (for Darcy's law, see Plate 4). In the following we are using stresses, pressure and strain not as absolute quantities but as excess quantities with regard to the equilibrium condition. Users of Hooke's law and consequently of poroelasticity are sometimes confused by an inconsistent use of signs for strain components: Whereas modellers in continuum mechanics take mechanical extension and the forces that lead to extension both positive, engineers in rock mechanics and seismologists note shortening and compression positive. As excess pore pressure P is positive in both communities, and so is increasing confining pressure P_c, the normalised sum of the normal stress components σ_{ii} making up P_c has a minus sign in continuum mechanics, but not in rock mechanics and seismology (Plate 8).

3.2. Governing equations

To obtain the fundamental equations of poroelasticity we first recall the respective equations of elasticity. Let us apply the concept of equilibrium conditions as illustrated in Plate 9. Then, solving the stress-strain relations of Hooke's law (Plate 7) for the normal and the shear stress components σ_{ij} and introducing those into the equilibrium conditions, we obtain the terms

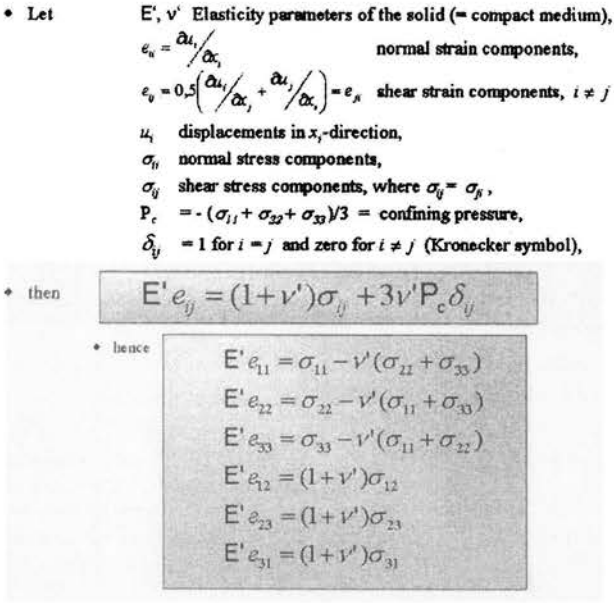

PLATE 7: Stress-strain relations for 3-D solids obeying Hooke's linear law of elasticity.

given on Plate 10, called governing equations of linear elasticity. Different from the elastic case, in poroelasticity we have a further variable i.e., the pore pressure P. It enters as a body force term in the equilibrium equations (pore pressure gradients in x_1, x_2, and x_3 directions) and as a temporal gradient as well as a Laplacian in a fourth equation. The latter has been derived in [4] by using a compressibility parameter Q^{-1} (see Plate 11). Applying the same transformations as in elasticity, we then obtain the governing equations for poroelastic media (Plate 12). There are five independent parameters in homogeneous, isotropic poroelastic material. The form noted in Plate 12 uses the drained Young's modulus E, the drained and undrained Poisson's ratios ν, ν_u, the Skempton ratio B, and the Darcy conductivity κ.

There is a remarkable coincidence between poroelasticity and thermoelasticity. Basically, the temperature in thermoelasticty takes a similar role as pore pressure in poroelasticity (Plate 13). However, as coupling between temperature and strain in most practical cases of thermoeleasticity is much weaker than coupling between pore pressure and strain in poroelasticity, many of the solutions applied in thermoelasticity can not be applied in poroelasticity: Solutions in thermoelasticity account for strain induced by changes in temperature, but disregard changes in temperature

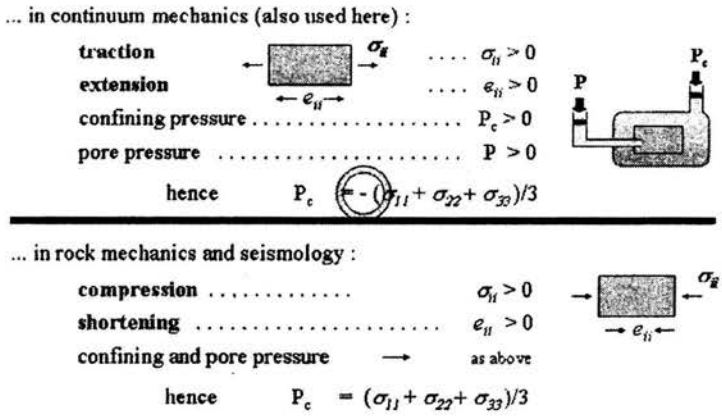

PLATE 8: Sign convention for stress, strain, and pressure common in continuum mechanics (top) and in rock mechanics as well as in seismology (bottom). e_{ii} denotes components of the strain tensor. Note minus sign in expression for P_c in continuum mechanics.

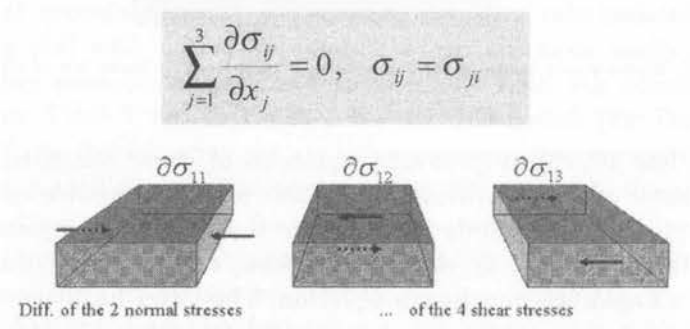

PLATE 9: Equilibrium conditions for a solid in short notation (top) with illustration for x_1 direction (bottom). The sum of the normal stress differences on the right and left hand sides of a solid element, of the shear stress differences of upper and lower sides, and of the shear stress differences of the front and back sides is zero, for all directions, respectively.

induced by strain. In poroelasticity, both, changes in strain induced by pore pressure fluctuations as well as changes in pore pressure induced by matrix strain have generally to be accounted for.

3.3. Further insight into poroelasticity

Some other considerations may help to better understand the physics of poroelasticity. As for transient phenomena, one may think of three processes

$$\frac{E'}{2(1+\nu')}\left(\nabla^2 u_i + \frac{1}{1-2\nu'}\frac{\partial \Delta_V}{\partial x_i}\right) = 0$$

where $\nabla^2 = \frac{\partial^2}{\partial x_1^2} + \frac{\partial^2}{\partial x_2^2} + \frac{\partial^2}{\partial x_3^2} = 0$

and $\Delta_V = e_{11} + e_{22} + e_{33}$

$$\mu'\nabla^2 u_i + \frac{\mu'}{1-2\nu'}\frac{\partial \Delta_V}{\partial x_i} = 0$$

PLATE 10: Governing equations for an elastic solid with u_i denoting the variables i.e., the displacements in directions x_i. The upper form is obtained by solving Hooke's law for σ_{ij} and application to the equilibrium conditions; the lower form results from substituting $E'/[2(1+\nu')]$ by μ'.

- E, ν replacing E', ν'
- right hand side not zero but = $\alpha\,\partial P/\partial x_i$, (body forces !) hence →

$$(i = 1,2,3) \qquad \mu\nabla^2 u_i + \frac{\mu}{1-2\nu}\frac{\partial \Delta_V}{\partial x_i} = \alpha\frac{\partial P}{\partial x_i}$$

- then P is new variable
- requires 4th equation →

$$\frac{1}{Q}\frac{\partial P}{\partial t} + \alpha\frac{\partial \Delta_V}{\partial t} = \kappa\nabla^2 P$$

where Q^{-1} is a compressibility parameter of Biot

$$\frac{1}{Q} = \frac{9}{2}\frac{(1-2\nu)(\nu_u - \nu)}{2(1-2\nu)(1+\nu_u)^2\mu B^2} = S - \alpha^2 c$$

PLATE 11: Governing equations for a poroelastic medium. Changes with respect to an elastic body are commented on the left.

playing different roles in redistribution of stresses and pressure: matrix deformation, diffusion of pore pressure, and fluid flow through the matrix. How are all these reflected in the governing equations?

When the initial (equilibrium) state is distorted, the mechanical deformation of the matrix occurs 'instantaneously'. However, as no deformation process can propagate at infinite velocity, instantaneous simply means that the deformation process is not resolved in time. The maximum possible velocity is in fact that of the seismic velocity; but propagation of

$$E e_{ij} = (1+\nu)\sigma_{ij} + \left[3\nu P_c + \frac{3(\nu_u - \nu)}{(1+\nu_u)B} P \right] \delta_{ij}$$

$$\frac{9(\nu_u - \nu)}{(1+\nu_u)EB} \frac{\partial (P/B - P_c)}{\partial t} = \kappa \nabla^2 P$$

PLATE 12: Stress-strain relations for a poroelastic medium in parameters E, B, ν, ν_u, and $\kappa(i = 1,2,3)$.

Temperature T takes similar role as pore pressure P:

- heating or pore pressure rise induce increase in volume
- instead of $\alpha \partial P/\partial x_i$ there is $(\beta/c') \partial T/\partial x_i$ (all in [Pa/m])

where β = thermal volume expansion coefficient

However: **Coupling in poroelasticity is stronger than in thermoelasticity (!)**

For instance: pore pressure change induces strain *and* vice versa; change in temperature induces strain, *but hardly* vice versa.

Hence, the 4 equations in poroelasticity must be solved together;
→ simplifying uncoupled solutions from thermoelasticity are generally *not* applicable.

PLATE 13: Correspondency of poroelasticity and thermoelasticity. The importance of coupling between strain and the additional variable (P or T) is much stronger in poroelasticity than in thermoelasticity. c' is the compressibility of the compact body in thermoelasticity.

seismic waves is not accounted for in the quasi-static terms presented above. Plate 14 summarizes the essentials for this case. What about fluid flow?

We may think of a tracer migrating through the permeable structure of the poroelastic body (Plate 15). Clearly, its propagation velocity depends on permeability, or hydraulic conductivity - quantities with values over a very wide range in natural materials [16, 17]. In principle, the process is described by Darcy's law. However, pure migration of fluid particles through the pore space does not contribute to deformation of the matrix. Darcy's law does not reveal how a pore pressure gradient is varying in response to fluid flow.

Third, we have pore pressure gradients. They explicitly occur as body forces in the governing equations (cf. Plate 11), so contribute to deformation and pore pressure changes in poroelastic media. The process is illustrated in Plate 16. To adjust a pore pressure disequilibrium in adjacent pores, only a small volume of the fluid within a pore of excess pressure needs to flow into a

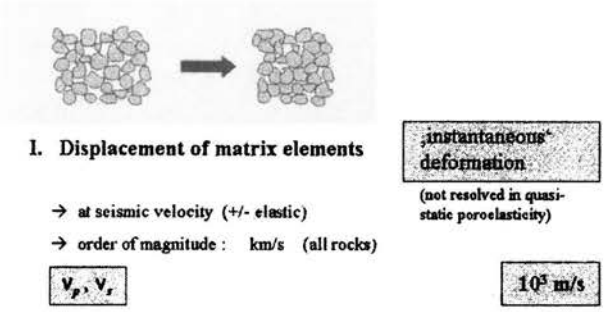

PLATE 14: Propagation of matrix deformation through poroelastic bodies in virtually no time ('instantaneously'). Real velocity of matrix element displacements is that of seismic waves i.e., v_p, v_s, of order km/s for rocks (as noted at lower right).

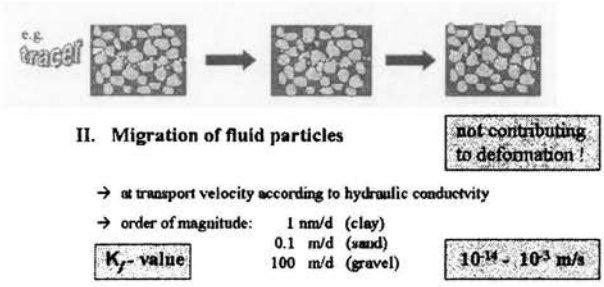

PLATE 15: Migration of fluid particles through porous media at 'transport' velocity i.e., permeability k or hydraulic conductivity K_f. Mere displacement of a fluid particle within the medium is neither associated with deformation of the matrix nor with a change in pore pressure; range of values at lower right.

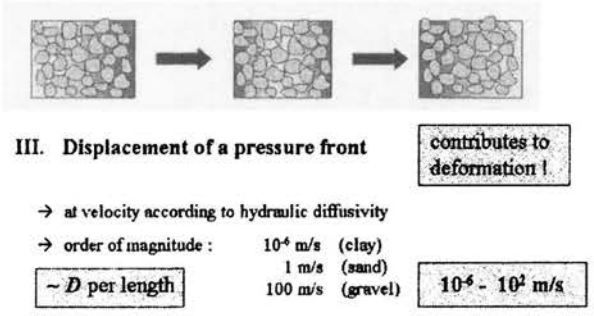

PLATE 16: Pore pressure disturbance passing through porous medium at velocity higher than that of transport of fluid particles; velocity corresponds to hydraulic diffusivity D per unit length (range of values at lower right).

neighbouring pore with deficit pressure. This type of flow is also governed by Darcy's law, yet, as the affected fluid volume is smaller than the total pore volume, the process can propagate much faster than fluid transport.

Another way of looking at a phenomenon is through schematics. Fig. 4 has classical examples for elasticity (spring), viscosity (dash pot), plasticity (slider block), and viscoelasticity (spring and dash pot in series). Can we imagine poroelasticity by a similar schematic? Fig. 5 shows an approach where the elastic and hydraulic properties

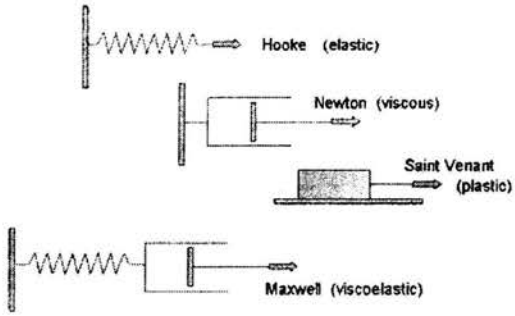

Figure 4: Schematics of Hooke, Newtonian, Saint-Venant and Maxwell rheologies.

are decoupled (separated elements).

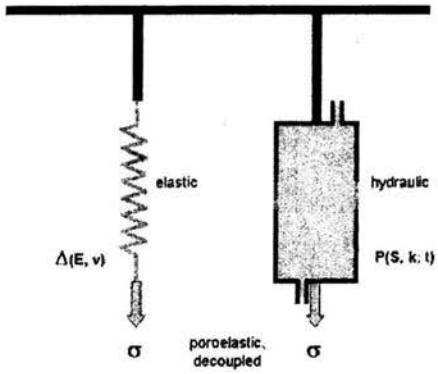

Figure 5: Schematics of a decoupled poroelastic approach; Young's modulus E and Poisson's ratio ν describe the elastic deformation Δ, storage compressibility S and permeability k stand for the hydraulic or pore pressure part P. In the time domain t, only the hydraulic part is accounted for. σ denotes normal stress (traction).

A better solution has Fig. 6. We may call the element a Biot-body since

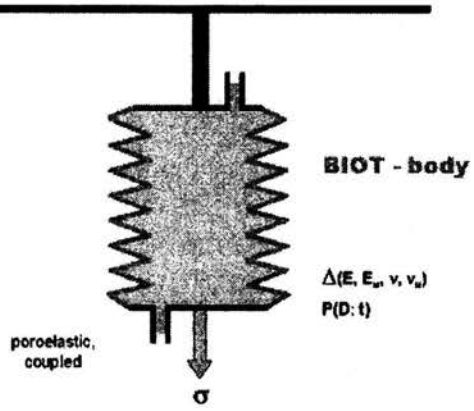

Figure 6: Schematics of a coupled poroelastic process (Biot-body). Young's moduli E, E_u and Poisson's ratios ν, ν_u dominate the elastic deformation Δ; hydraulic diffusivity D governs the hydraulic part P, which is fully resolved in time t. Yet, as poroelasticity is a strongly coupled rheology, changes in Δ and P occur simultaneously.

it represents characteristics of three-dimensional poroelasticity (as 2-D cut). The matrix deformation Δ and the hydraulic part P may, for instance, be expressed by use of Young's modulus and Poisson's ratio, both drained and undrained, and by hydraulic diffusivity D. Using the Biot-body, drained and undrained conditions can easily be illustrated (Fig. 7).

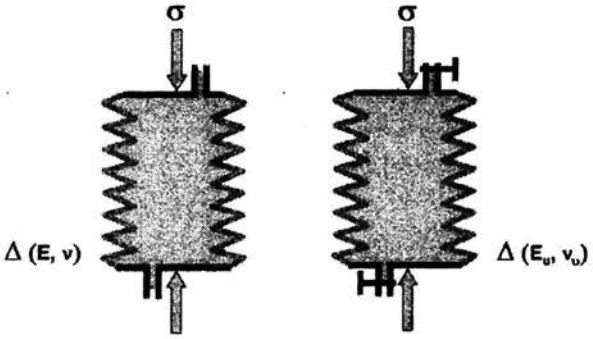

Figure 7: Drained (left) and undrained (right) conditions with respective characteristic parameters governing matrix deformation Δ.

Similarly, the meaning of the Skempton ratio B can be visualized, as can the fact that the shear modulus μ does not depend on the conditions of drainage (Fig. 8).

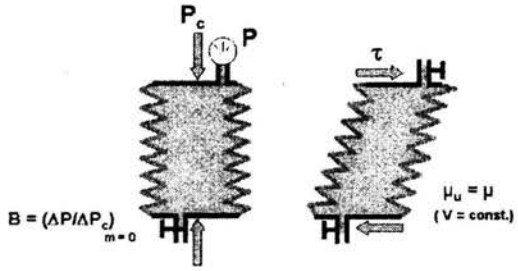

Figure 8: Definition of Skempton ratio B (left) and illustration of independence of the volume of a poroelastic sample from its state of shear deformation, regardless of the conditions of drainage (shown for drained condition; right). In the latter case, the volume would not change if the in-/outlets were locked, i.e. for undrained condition.

4. Some fundamental solutions

4.1. Axisymmetric problems in poroelasticity

As for hydrological applications of poroelasticity, practical problems are often related to wells or boreholes: Ground water is extracted from aquifers through boreholes; fluids are injected through boreholes into underground formations; in-situ pore pressure fluctuations are observed by means of wells. In all cases, cylindrical coordinates are best suited to describe the process mathematically.

Because of the strong coupling between deformation and pore pressure in poroelasticity, analytical solutions of the governing equations are known for rather elementary boundary conditions only; e.g., point source solutions for deviations from the equilibrium conditions in the isotropic, homogeneous full space. As the theory is linear, the analytical expressions present fundamental solutions which can be stacked to simulate more complex situations. An example is shown in Fig. 9. In the following, fundamental solutions for two particular situations in poroelasticity are presented: The first is the one illustrated in Fig. 9, the second one will be the point source solution for an instantaneously beginning, steadily ongoing injection of fluid volume (e.g, a negative yield pump test). We will consider the pore pressure and the deformation fields in the vicinity of the point source, respectively (originally in [18]). Fig. 10 and Plate 17 have the four components of the deformation tensor that we will be interested in.

4.2. Impuls-like injection of a finite fluid volume

When a fluid mass m_f of density ρ_f is instantaneously injected at time t=0 through a point source at the origin of a homogeneous, isotropic poroelastic full space, the governing equations can be used to compute the solutions $P(r, z; t)$ and stresses $\sigma_{ij}(r, z; t)$ at distance R from the source. The solutions are noted in Plate 18.

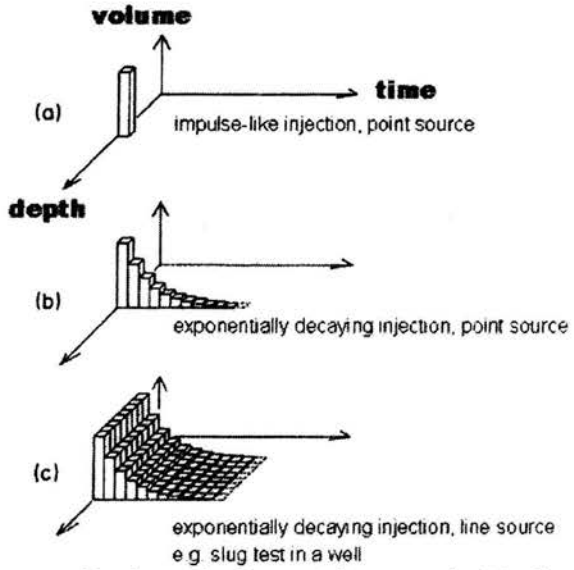

Figure 9: Relevance of fundamental solutions in linear poroelasticity for application of its differential equation system to a hydrological problem. (a) Fundamental solution for an instantaneous, impulse-like injection of some finite fluid volume at a certain depth of a well. (b) Superposition of solutions (a) to mimic an exponential decay of the injection process. (c) Superposition of solutions (b) to simulate an exponentially decaying injection of a fluid volume through a finite-length cylindrical well screen.

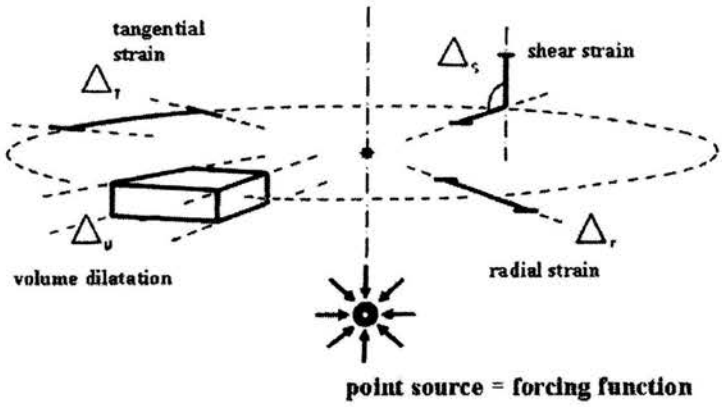

Figure 10: Strain components for axisymmetric problems: volume strain Δ_V, radial strain Δ_r, shear strain Δ_S, and tangential strain Δ_T.

- **general :**

$$\Delta_V = e_{rr} + e_{\theta\theta} + e_{zz} = \frac{\partial u_r}{\partial r} + \frac{1}{r}\left(\frac{\partial u_\theta}{\partial \theta} + u_r\right) + \frac{\partial u_z}{\partial z}$$

$$\Delta_r = e_{rr} = \frac{\partial u_r}{\partial r}$$

$$\Delta_T = e_{\theta\theta} = \frac{1}{r}\left(\frac{\partial u_\theta}{\partial \theta} + u_r\right)$$

$$\Delta_S = e_{rz} = \frac{1}{2}\left(\frac{\partial u_z}{\partial r} + \frac{\partial u_r}{\partial z}\right)$$

- **for axial symmetry :**

$$\left.\begin{aligned} \Delta_V &= \frac{\partial u_r}{\partial r} + \frac{u_r}{r} + \frac{\partial u_z}{\partial z} \\ \Delta_T &= \frac{u_r}{r} \end{aligned}\right\} \quad \text{as} \quad \frac{\partial u_\theta}{\partial \theta} = 0$$

PLATE 17: Strain components in cylindrical coordinates r, θ, z; complete form (top) and for axial symmetry (bottom). u_r, u_θ, u_z denote displacements in r, θ, z directions.

- Assumption : State of equilibrium (influence of previous disturbances has fully decayed)
- Forcing : Injection of fluid mass m_f at time t=0, corresponds to fluid volume $V_f = m_f/\rho_f$ at t=0
- Solution :

$$P = \frac{V_f}{8\pi R\kappa t}\Re\dot{\epsilon} = \frac{D}{\kappa\overline{B}}M\Re\dot{\epsilon}$$

$$\sigma_{ij} = 2\mu M\left[(\Im - \Re\dot{\epsilon})\delta_{ij} - \frac{x_i x_j}{R^2}(3\Im - \Re\dot{\epsilon})\right]$$

$$R = \sqrt{r^2 + z^2} \quad [m]$$

$$\Re = \frac{R}{2\sqrt{Dt}} \quad [-]$$

$$M = \frac{V_f \overline{B}\Re^2}{2\pi R^3} = \frac{V_f \overline{B}}{8\pi RDt} \quad [-]$$

$$\overline{B} = \frac{B}{3}\frac{1+\nu_u}{1-\nu_u} \quad [-]$$

$$\epsilon = erf(\Re) = \frac{2}{\sqrt{\pi}}\int_0^{\Re}\exp(-s^2)ds \quad [-] = \text{error function}$$

$$\dot{\epsilon} = \frac{d\epsilon}{d\Re} = \frac{2}{\sqrt{\pi}}\exp(-\Re^2) \quad [-]$$

$$\Im = \frac{\epsilon\,\Re - \dot{\epsilon}}{2\Re} \quad [-]$$

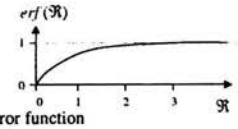

PLATE 18: Solutions for pore pressure P and stresses σ_{ij} at distance R and time t after impulse-like injection of fluid volume V_f through point source in poroelastic medium, characterized by parameters μ, ν, ν_u, B, D (and κ). The solutions are presented by use of dimensionless quantities noted in the lower part.

Application to the stress-strain relations of poroelastic media (cf. Plate 12) and solving for the strain components Δ_V, $\Delta_{r,0}$, Δ_S, Δ_T yield the expressions given in Plate 19. Note that $\Delta_V$is proportional to pore pressure P. The behaviour of the strain components as functions of distance from the point source is shown in Fig. 11.

$$\Delta_V = M\,\Re\dot{\epsilon} = \frac{\kappa\overline{B}}{D}P$$

$$\Delta_S = -M\,\frac{2rz}{R^2}\,\frac{(3\Im-\Re\dot{\epsilon})}{2}$$

$$\Delta_{r,0} = M\left[\Im-\frac{r^2}{R^2}(3\Im-\Re\dot{\epsilon})\right]$$

$$\Delta_T = M\,\Im$$

PLATE 19: Strain components for problem given in Plate 18. Note that $\Delta_{r,0}$is the radial strain at depth z=0 i.e., at the depth of the point source. (The term $\Delta_r$is more complex.)

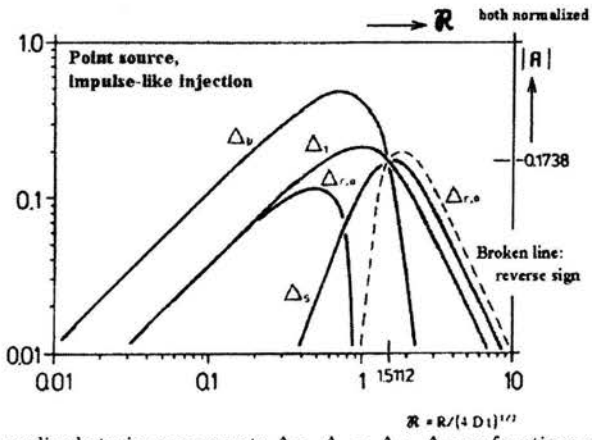

Figure 11: Normalized strain components Δ_V, $\Delta_{r,0}$, Δ_S, Δ_T as functions of dimensionless distance $R/(4Dt)^{1/2}$ as noted in Plate 21. All solutions take the amplitude 0.1738 at distance 1.5112. Pore pressure P has the same behaviour as volume dilatation Δ_V.

4.3. Suddenly starting, steadily ongoing injection of fluid volume

When a fluid mass m_f of density ρ_f is injected at constant rate Q_f through a point source at the origin of a homogeneous, isotropic poroelastic full space, the governing equations can again be used to compute the solutions $P(r, z; t)$ and stresses $\sigma_{ij}(r, z; t)$ at distance R from the source. Let the injection begin at time t=0. The situation is typical for a pump test in hydrology or in the oil industry for reservoir assessment - with negative injection rate. The solutions are noted in Plate 20.

- Assumption : State of equilibrium (influence of previous disturbances has fully decayed)
- Forcing : Constant injection rate Q_f beginning at time t=0, corresponds to fluid volume rate $V_f/t = m_f/(\rho_f t)$
- Solution :

$$P = \frac{Q_f}{4\pi R\kappa}\epsilon^- = \frac{D}{\kappa \bar{B}} M^* \epsilon^-$$

$$\sigma_{ij} = \mu M^* \left[(\Im - \epsilon^-)\delta_{ij} - \frac{x_i x_j}{R^2}(3\Im + \epsilon^-) \right]$$

$$R = \sqrt{r^2 + z^2} \quad [m]$$

$$\Re = \frac{R}{2\sqrt{Dt}} \quad [-]$$

$$M^* = \frac{Q_f \bar{B}}{4\pi R D} \quad [-]$$

$$\bar{B} = \frac{B}{3}\frac{1+\nu_u}{1-\nu_u} \quad [-]$$

$$\epsilon = erf(\Re) = \frac{2}{\sqrt{\pi}}\int_0^{\Re} \exp(-s^2)ds \quad [-]$$

$$\epsilon^- = 1 - erf(\Re) = erfc(\Re) \quad [-]$$

$$\Im = \frac{\epsilon - \Re\dot{\epsilon}}{2\Re} \quad [-]$$

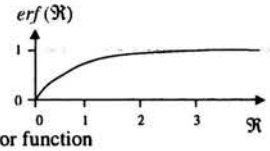

= error function

PLATE 20: Solutions for pore pressure P and stresses σ_{ij} at distance R and time t after sudden onset of injection of fluid volume V_f at constant rate Q_f through point source in poroelastic medium, characterized by parameters μ, ν, ν_u, B, D (and κ). The solutions are presented by use of dimensionless quantities noted in the lower part.

Application to the stress-strain relations of poroelastic media (cf. Plate 12) and solving for the strain components Δ_V, $\Delta_{r,0}$, Δ_S, Δ_T yields the

expressions given in Plate 21.

$$\Delta_V = M^* \epsilon^- = \frac{\kappa \bar{B}}{D} P$$

$$\Delta_S = -M^* \frac{2rz}{R^2} \frac{(3\Im + \epsilon^-)}{4}$$

$$\Delta_{r,0} = \frac{M^*}{2} \left[(\Im + \epsilon^-) - \frac{r^2}{R^2} (3\Im + \epsilon^-) \right]$$

$$\Delta_T = \frac{M^*}{2} (\Im + \epsilon^-)$$

PLATE 21: Strain components for problem given in Plate 20. Note that $\Delta_{r,0}$ is the radial strain at depth z=0 i.e., at the depth of the point source. (The term Δ_r is more complex.)

Again, Δ_V is proportional to pore pressure P, which is in fact generally the case. The behaviour of the strain components as function of distance from the point source is shown in Fig. 12. Solving the dimensionless

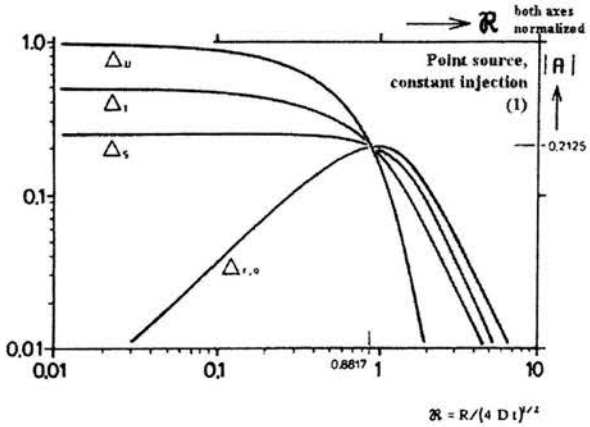

Figure 12: Normalized strain components Δ_V, $\Delta_{r,0}$, Δ_S, Δ_T as functions of dimensionless distance $R/(4Dt)^{1/2}$ as noted in Plate 21. All solutions take the amplitude 0.2125$\tilde{E}$ at distance 0.8817$\tilde{E}$. Pore pressure P has the same behaviour as volume dilatation Δ_V.

distance $R/(4Dt)^{1/2}$ for dimensionless time $4Dt/R^2$, the results can be plotted as function of the temporal evolution of the strain. Fig. 13 reveals that $\Delta_{r,0}$ passes through a maximum whereas the other strain components asymptotically approach a saturation which is attained after infinite duration of injection only. Evolutions of the 1-D strain components $\Delta_{r,0}$, Δ_S, Δ_T are faster than those of Δ_V and pore pressure P. This is also evident from the

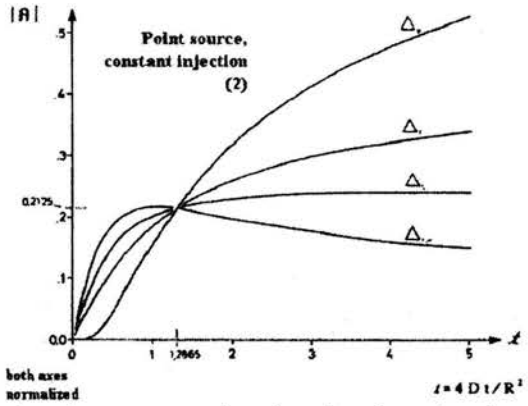

Figure 13: Normalized strain components Δ_V, $\Delta_{r,0}$, Δ_S, Δ_T as functions of dimensionless time $4Dt/R^2$as noted in Plate 21. All solutions take the amplitude 0.2125Ĕ at time 1.2865Ĕ . Pore pressure P has the same behaviour as volume dilatation Δ_V.

non-zero values of the time derivatives of $\Delta_{r,0}$, Δ_S, Δ_T at t=0, the graphs of which are plotted in Fig. 14. Obviously, changes in the 1-D strain components

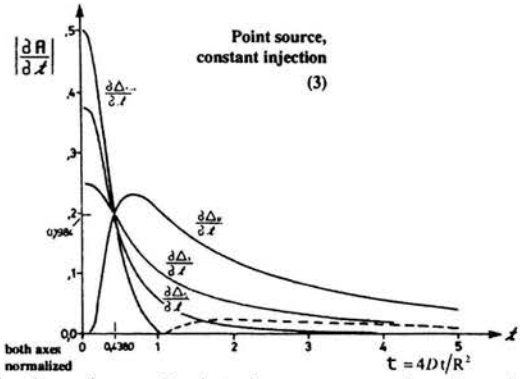

Figure 14: Time derivatives of normalized strain components Δ_V, $\Delta_{r,0}$, Δ_S, Δ_T as functions of dimensionless time $4Dt/R^2$ as noted in Plate 21. The derivative of radial strain $\Delta_{r,0}$ changes its sign for larger times (represented as broken line). All solutions pass through the same amplitude per time unit, 0.1984Ĕ, at time 0.4380Ĕ . Time derivative of pore pressure P has the same behaviour as that of volume dilatation Δ_V.

propagate at higher velocity in poroelastic media than volume dilatation or pore pressure. Moreover, the passing of all graphs through one point appears to indicate an invariant in the solutions (Figs. 12, 13, 14; and Fig. 11).

4.4. 2-D visualization of suddenly starting, steadily ongoing pumping

More realistic situations than the point source solutions described in sections 4.2 and 4.3 can be obtained through superpositions as mentioned in section 5.1. This holds for a more complex geometry and time function of the forcing source. However, in cases like a half space, a layered medium, or presence of other heterogeneities, numerical solutions of the governing equations are generally the only way to arrive at meaningful results. In Figs. 15 and 16, finite element modelling has been used to image the temporal evolution of poroelastic deformation and displacements in the r-, z-plane for two simple cases. (The first of the three plotted time steps is taken shortly after initiation of the distortion; the last one is taken when saturation of the shear strain response is nearly achieved; the second one is from in-between.) Fig. 15 presents again the solution of section 4.3. (Actually, in this case,

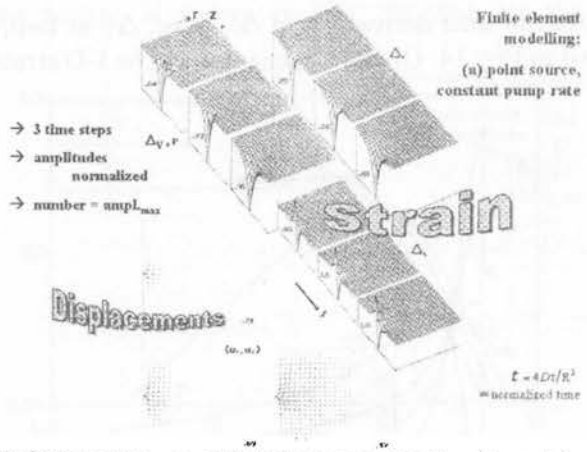

Figure 15: Displacements u_r, u_z and strain components Δ_V, Δ_S and Δ_r at three of six consecutive time steps (from top left to bottom right, respectively) in isotropic homogeneous poroelastic medium for sudden start of constant rate pumping through quasi point source (in centre of left margins). Results are obtained by finite element modelling. Amplitudes are normalized to maximum values of each scene, with size of the maximum value being indicated, respectively (in arbitrary units of displacements or strain); from [18].

the analytical solution can be used to verify the accuracy of the numerical results.) It can be seen, how the model region is increasingly affected by the process of the pumping namely, how the displacements are initially concentrated around the source and then invade into the cylindrical region.

Whereas the strains Δ_V and Δ_r look rather similar in type, shear strain Δ_S presents two distinct peaks of opposite sign - above and below the point source.

Fig. 16 shows the poroelastic behaviour in response to a line source pumping above a non-permeable layer. The effect of the source extension is visible from the elongated distortion along the axis and from greater separation of the two Δ_S peaks of different sign - the lower one of which is stronger because of a fixed boundary condition. The situation is typical for fluid withdrawal from an aquifer.

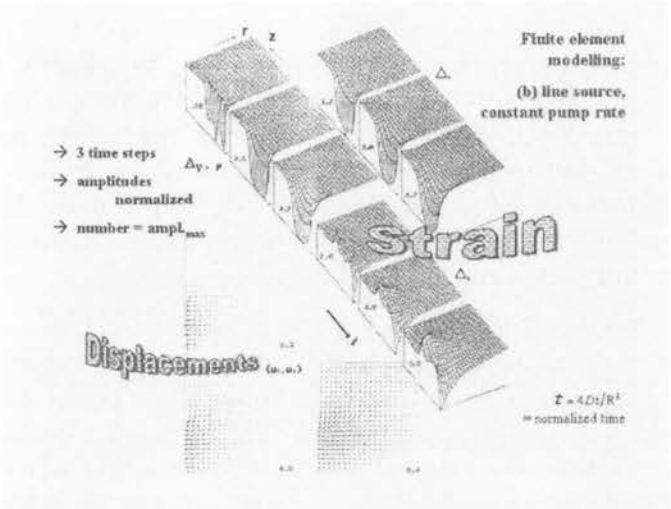

Figure 16: Same as Fig. 15 but for sudden start of constant rate pumping through quasi line source along axis of lower part of the model region above non-permeable layer.

5. Field cases of poroelasticity

5.1. Techniques of in-situ monitoring of poroelastic phenomena

Investigations into poroelastic phenomena e.g., to quantify poroelastic parameter values, require observations, either in the laboratory or in the field. In principle, it will be sufficient to monitor the forcing function and the response of the medium i.e. the change in pore pressure and/or in strain. We here focus on the field scale which is the more difficult task because less control is generally given over boundary conditions and possible heterogeneity of the medium than in the laboratory.

Fig. 17 illustrates four situations in which various combinations of types of forcing and monitoring are shown: The forcing can act either directly on the pore fluid or directly on the matrix; monitoring can be by observation of changes in pore pressure or in matrix strain. The indicated resolution required to 'see' the poroelastic effect is typical for natural geological formations when the strength of the forcing and distance between observation point and forcing are 'reasonable' ($1\mu\varepsilon = 10^{-6}$). The values may serve as a gross orientation. In reality, in-situ pore pressure changes can be observed by monitoring variations of the height of a well water table (= well level fluctuation), provided the well is open to the formation to be considered and the density of the fluid in the well is constant and is identical to that of the pore fluid. The situation is sketched in Fig. 18.

As we are interested in time dependent processes, the mean absolute well level height, reflecting the absolute pore pressure in the formation, is generally not of importance. Rather, we are interested in well level changes $\Delta h(t)$. A pressure sensor fixed at some depth below the well level will render readings that are proportional to the actual pore pressure in the formation. Hydraulic diffusivity of the probed formation should, however, be sufficiently high to allow for pressure adjustment between the pore pressure in the formation and the pressure of the water column in the well.

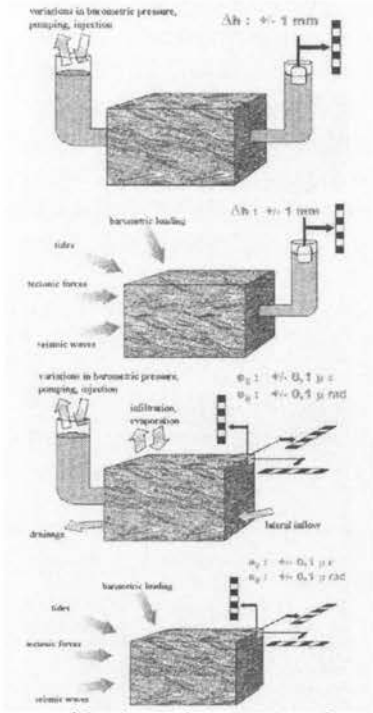

Figure 17: Four combinations of forcing and monitoring of poroelastic phenomena: Pore pressure change observed as pore pressure disturbance (top), matrix deformation observed as pore pressure disturbance (2^{nd} from top), pore pressure change observed as matrix strain (3^{rd} from top), and matrix deformation observed as matrix strain (bottom). Forcing sources are typical for the field scale and are meant as examples only. Monitoring of poroelastic effects requires resolutions as indicated (after [19]).

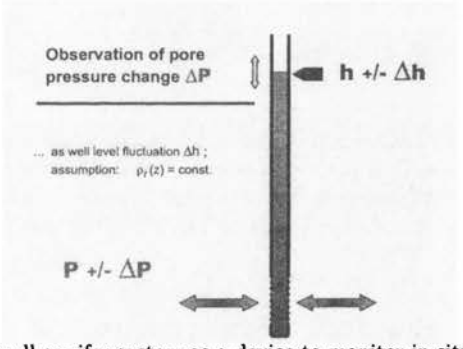

Figure 18: Sketch of a well aquifer system as a device to monitor in-situ pore pressure changes $\Delta P(t)$ through well level fluctuations $\Delta h(t)$. The well water has access to the aquifer through the open section (well screen). $\Delta h(t)$ can be recorded by means of a pressure sensor lowered into the water column.

A system more pressure sensitive than an open well would be a locked well i.e., a well that is sealed below the minimum height of its well level. In this case, pore pressure changes lead to equivalent changes in the pressure of the well water column with much reduced pore fluid flow. A pressure sensor then needs, however, to be installed below the sealing. As pore pressure is proportional to volume dilatation, a suitable well-aquifer system with pressure recording facility can also be regarded as a volume strainmeter.

Fig. 19 presents a method to observe in-situ matrix deformation by means of a tiltmeter. As tiltmeters are sensitive to both shear strain Δ_S and rotation, the latter quantity has to be assessed separately if relevant. Shear strains are partly transferred into rotations close to material boundaries, in particular close to the stress free surface (also known as strain-tilt coupling). The effect can be accounted for by numerical modelling when values of material parameters are known. Tiltmeters of resolution 0.1 μrad are readily available; some even attain 1 $nrad$ (equivalent to 0.2 milliseconds of arc) but are more difficult to handle.

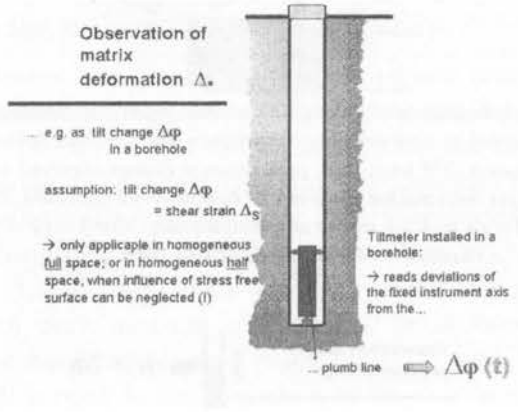

Figure 19: Sketch of tiltmeter installation in a borehole for monitoring in-situ matrix deformation $\Delta_\bullet$ in response to a change in poroelastic strain. Tiltmeters are sensitive to shear strain Δ_S and to rotations. Changes in vertical tilt are sensed with reference to the plumb line (which is different from the axis of the borehole!).

Instead of using tiltmeters, linear strainmeters of minimum resolution $0.1\mu\varepsilon$, e.g. in radial and/or tangential direction of a well, can likewise be used to observe in-situ matrix deformation (e.g. [20]). Instruments with base lengths exceeding a few decimetres can usually be installed only near the surface, or in a mine. Volume strain Δ_V can also be monitored

namely, by means of borehole dilatometers. In general, borehole versions of strainmeters (linear or volume) are technically more sophisticated than borehole tiltmeters.

5.2. Inverse well level response - Noordbergum effect

Let us come back to the case study presented in Fig. 1. To understand the phenomenon called Noordbergum effect we may think of the following problem: Suppose we have an impermeable poroelastic medium, e.g. of material used for wet-swimsuits (neoprene). A fluid volume V shall be injected into a circular hole of the medium. What will be the change in pore pressure inside a pore at some distance from the injection hole when (a) the medium is infinite, and (b) the medium is a sphere with a free surface at some finite radius (Fig. 20)?

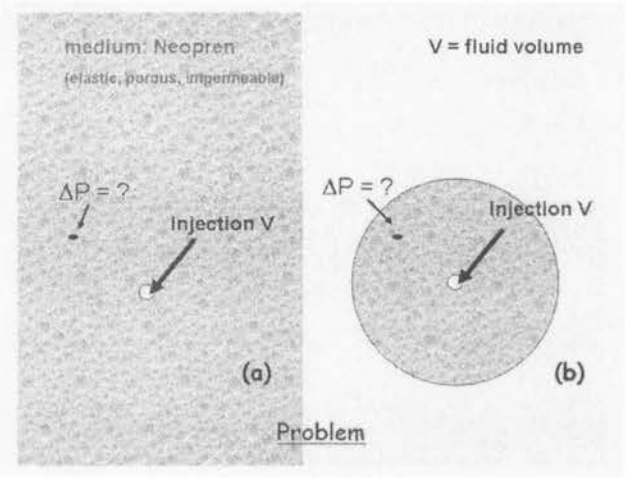

Figure 20: Let some fluid volume V be injected into a circular hole in an impermeable porous elastic material (e.g. neoprene). What would be the pore pressure change ΔP in the vicinity of the injection hole when the medium is infinite (a) or a sphere (b)?

In case of problem (a) we will argue that the injection hole will inflate and thereby compress its surrounding. Compression of pores will be less at greater than at shorter distance from the injection point; but whatever the distance is, the pore pressure will rise by some amount, so $\Delta P > 0$ (Fig. 21). Intuitively, for problem (b), we might expect the same result. However, at a second thought, we may realize that the free surface of the sphere does

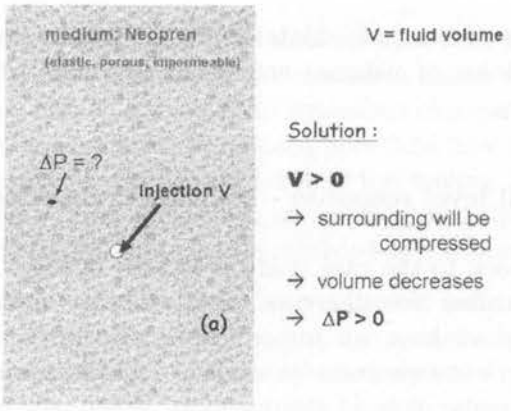

Figure 21: Solution of problem (a) of Fig. 20.

not pose a radial resistance to the inflation in the centre (Fig. 22). There

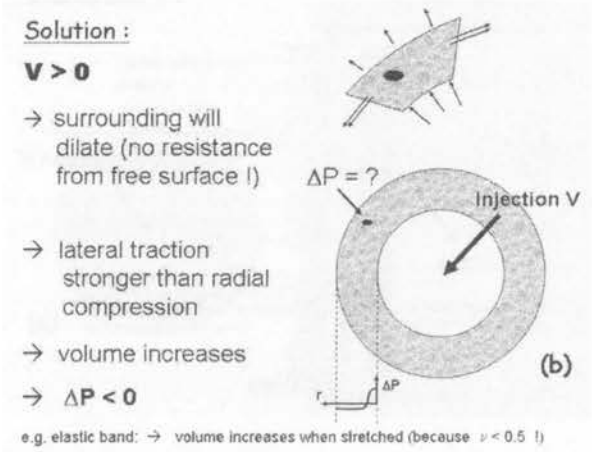

Figure 22: Solution of problem (b) of Fig. 20.

will mainly be tangential, extensional forces, leading to the so-called hoop strain which will override the radial compression (except for the innermost part of the sphere). The situation becomes clearer if we assume the injection hole to be rather large in relation to the whole sphere. Like with a stretched elastic band, the total volume of our impermeable material will increase. Accordingly, the pores' volumes in most parts of the sphere will increase; hence the pore pressure in these pores will decrease.

If for case (b) the medium would be permeable we can distinguish two phases of pressure readjustment after fluid injection: Initially, the situation would be similar as mentioned before, because the response of the matrix would be 'instantaneous' (in the sense of Plate 14). Then, permeability allows the elevated pore pressure from the injection hole to diffuse into the medium and, by time, will overcompensate the initial pore pressure drop. This describes the inverse well level effect of Fig. 1. The phenomenon is particularly strong when a low permeable layer (aquiclude) separates the pumped aquifer from the one in which the inverse pore pressure response is observed. This is the case for the recordings shown in Fig. 1, and was also reported for the Noordbergum effect [2]. The field case is an example for the situation sketched in the uppermost picture of Fig. 17.

5.3. Loading, tidal, and barometric efficiencies

There are various types of natural forcing that provoke poroelastic reactions in geological formations. These are surface loading e.g., from rainfall, snow cover, or marine tides in coastal areas; earth tidal strain; and barometric effects. Evidence of the effects is obtained from analysis of well level fluctuations in boreholes (cf. two top pictures of Fig. 17). It is, however, essential that the wells tap aquifers that are *confined*. A confined aquifer is a permeable, ground water saturated layer which is covered by a non- or low-permeable layer, named aquiclude, and that is fully submerged below the free water table (Fig. 23). Alternatively, the aquifer may be so

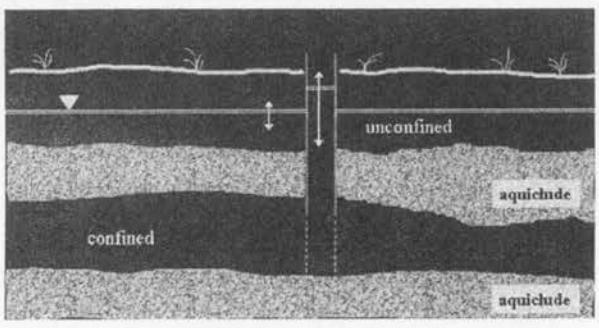

Figure 23: Confined and unconfined aquifers. White triangle marks depth of free water table. Heights of free water table and of water level in borehole connected to a confined aquifer generally differ from each other.

deep that adjustments of local pore pressure anomalies via displacements of the free water table would be strongly delayed. Any deep aquifer can thus be considered as a confined one. Aquifers at shallow depths require an even shallower aquiclude to be confined. When a borehole is hydraulically connected to a confined aquifer, level fluctuations in the well will differ from those of the free water table.

As a field example, we consider well level recordings obtained in the pilot hole of KTB (= Kontinentales Tiefbohrprogramm), Germany's superdeep drilling project. The pilot hole, named KTB-VB, reaches 4000 m depth and is open in its lowermost 150 m (see Fig. 24; both, KTB-VB and the 9101 m deep main hole, KTB-HB, were drilled in crystalline rock). Because of the great depth of the borehole's open section, the rock-fluid regime connected to KTB-VB can be regarded as confined.

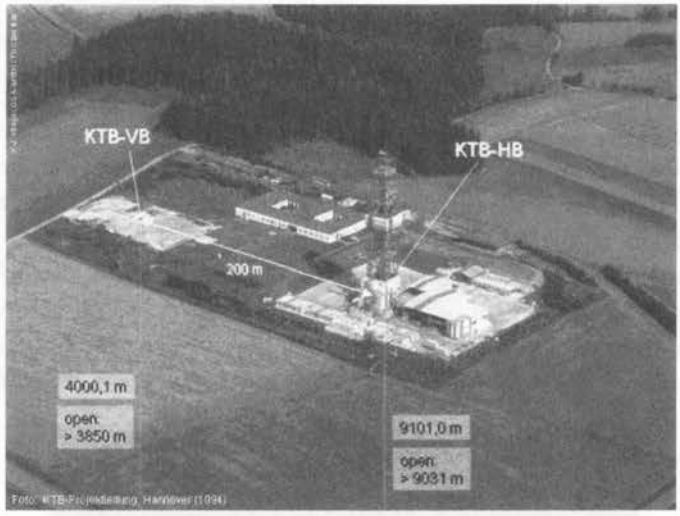

Figure 24: Site of the two drill holes of KTB, the 4 km deep pilot hole KTB-VB and the 9.1 km deep main hole KTB-HB, in Oberpfalz region, Bavaria. The boreholes are at 200 m surface distance from each other. They are fully cased except for the lowermost parts as indicated.

The fluid level recording, shown in Fig. 25, presents fluctuations in the centimetre to decimetre range. At closer look, the fluctuations can be recognised as being anti-correlated to changes in barometric pressure. Moreover, when the barometric-type fluctuations are removed by regression analysis, the residual signal shows systematic variations strongly correlated to areal earth tidal strain. Given that the recording of pore pressure variations

at 3.85 to 4 km depth shows influence of barometric pressure variations and of earth tides, and that these signals are well known from surface registrations and theory, we can imagine of using this information for assessing certain in-situ rock parameters from analysing the well level curve.

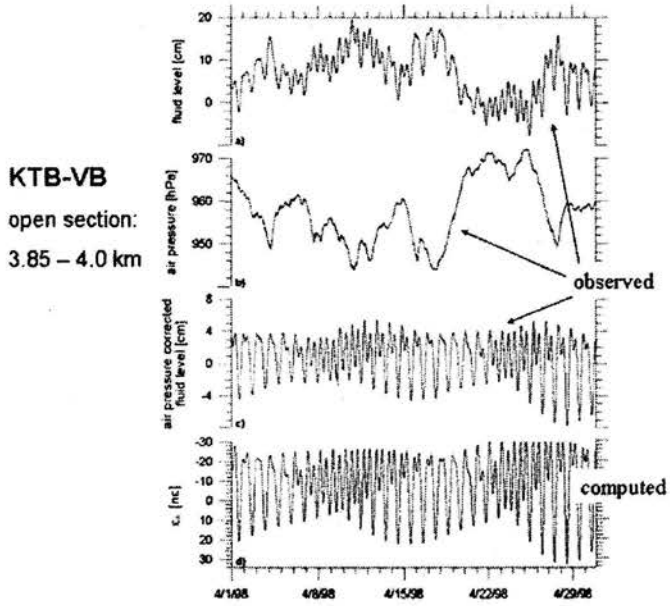

Figure 25: One month of time series from KTB-VB: a) well level recording, b) barometric fluctuations, c) fluid level recording with barometric effects removed, d) theoretical areal earth tide strain for KTB location in units of nano-strain ($n\varepsilon$); observational data set after [21], theoretical tide after [22] .

The way how such rock parameter values can be deduced is explained in Plates 22 to 26. It is thereby assumed that the zone affected by pore pressure changes reacts linearly poroelastic to external forcing, the region is homogeneous, and the fluid level in the borehole reflects pore pressure conditions in the connected formation without much delay. The latter assumption requires hydraulic conductivity to be sufficiently high. Otherwise a formulation accounting for the transient character of the well level response following a change in pore pressure has to be applied (e.g. [23]). It has to be admitted that the aforementioned conditions are quite idealistic. Therefore, it would be better to consider the deduced parameter values as effective medium parameters. Nevertheless, the technique presents a simple and cost-

effective way to quantify in-situ parameter values that are not easily obtained through other methods.

Plate 22 presents the situation for surface loading and is self-explanatory. The loading efficiency L_e is a dimensionless factor expressing to what extent

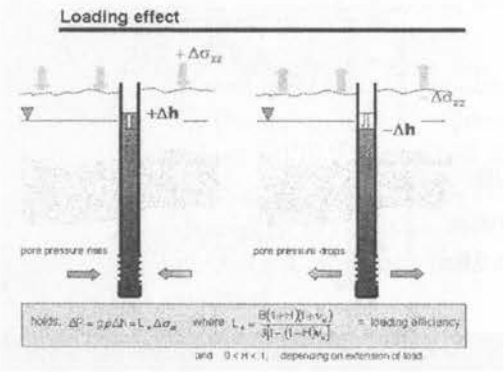

PLATE 22: Loading effect and loading efficiency L_e as function of poroelastic parameters B and ν_u. Positive surface loading $\Delta\sigma_{zz}$ compresses the matrix, provoking a pore pressure rise ΔP which leads to a rise of the well level by Δh, and vice versa, respectively. H is a dimensionless coefficient introduced by [24], accounting for the ratio of areal to vertical strain induced by a load (H=0 is the traditional assumption in hydrology of vertical strains only; H=1 holds for finite though extended loads on the half space).

a supplementary surface load is reflected in the pore pressure. Plate 23 has the case of tidal forcing. The causative orbital movements of earth, moon,

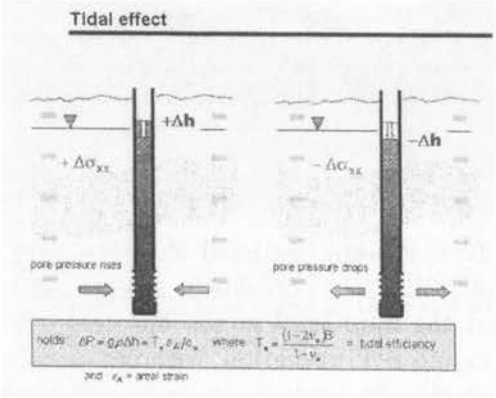

PLATE 23: Earth tidal squeezing and tidal efficiency T_e as function of poroelastic parameters B and ν_u. Compression $\Delta\sigma_{xx}$ of the matrix provokes a pore pressure rise ΔP leading to a rise of the well level by Δh, and vice versa. Tidal signals unveil themselves by characteristic frequencies in diurnal and semi-diurnal bands. The coefficient of B in the expression for T_e is $\varepsilon_V/\varepsilon_A$ (= ratio of volume strain ε_V to areal strain ε_A).

and sun are well known from astronomy, and so is the spectrum of tidal

forces [25]. Less known, due to uncertainties of rock formation rigidities, is the local deformation of the earth, as the induced areal strain tide ε_A [26, 27]. Yet, the dimensionless tidal efficiency T_e deduced from the ratio of induced pore pressure change ΔP (multiplied by undrained compressibility c_u) and the estimated areal tidal strain ε_A indicate to what extent tidal matrix deformation is transferred into pore pressure change. Then, Plates 24 to 26 illustrate the barometric effect and how this is made up of pure matrix loading and loading directly on the well water column. The dimensionless

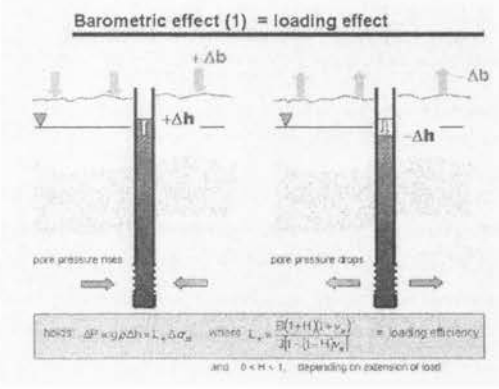

PLATE 24: Matrix loading part of the barometric effect with loading efficiency L_e as explained in Plate 22. The load $\Delta\sigma_{zz}$ is the change in local air pressure, Δb.

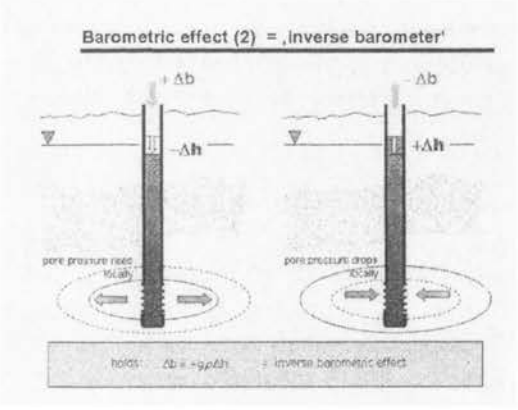

PLATE 25: Direct loading of the well water column by changes in barometric pressure Δb, also called inverse barometric effect. For a rise in local air pressure Δb, the well level drops because well water is forced into the connected formation, and vice versa.

barometric efficiency A_e reveals to what extent a change in air pressure is reflected in the pore pressure of the studied formation.

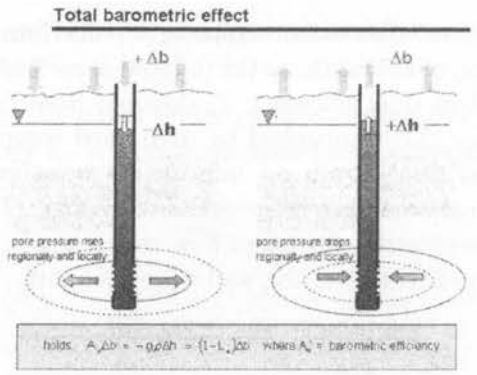

PLATE 26: Superposition of matrix loading and inverse barometric effect yielding total barometric effect with barometric efficiency $A_e = 1-L_e$.

Fig. 26 shows how T_e and A_e can be used to quantify in-situ rock parameters (here for KTB-VB). The upper diagram is a plot of B over ν_u with isolines for L_e (i.e. $B=3L_e/[2(1+\nu_u)]$, assuming H=1; see Plates 22, 24). Values for $L_e = 1-A_e$ result from analysis of the observed barometric efficiency A_e, yielding $0.35 < L_e < 0.40$. As the undrained Poisson's ratio ν_u is confined to a range of 0.25 to 0.35 from other considerations, there is a limited range for values of the Skempton ratio B, namely 0.39 to 0.48. The lower diagram presents B over undrained compressibility c_u with isolines for the volume strain sensitivity, A_V (i.e. $B=A_V c_u$). A_V is related (a) to L_e through $A_V = 2(1-\nu_u)\mu L_e/(1-2\nu_u)$, where $(1-\nu_u)/(1-2\nu_u)$ is the ratio of volume to areal strain sensitivity; or of volume to areal strain, $\varepsilon_V/\varepsilon_A$; and (b) to T_e via the relation $A_V = [(1-\nu_u)T_e]/[(1-2\nu_u)c_u]$ (cf. Plate 23; see also [24]).

5.4. Poroelastic deformation through pumping

Let us next consider cases of the type presented in the two lowermost pictures of Fig. 17. Fig. 27 shows signals of a highly sensitive borehole tiltmeter (type ASKASNIA vertical pendulum) that were recorded in a quaternary sand formation at 30 m depth, near a village named Medelby, Northern Germany [18]. The two curves in each diagram are tilt signals in two perpendicular directions, X and Y. The orientation of the tiltmeter relative to North is different for each diagram (see insets on right). Signal amplitudes for X and Y can be seen from the 50 nrad marks (about 10 mseca) on the left, respectively. The curves present two types of phenomena: A smooth, almost sinusoidal variation and a number of jagged anomalies which occur

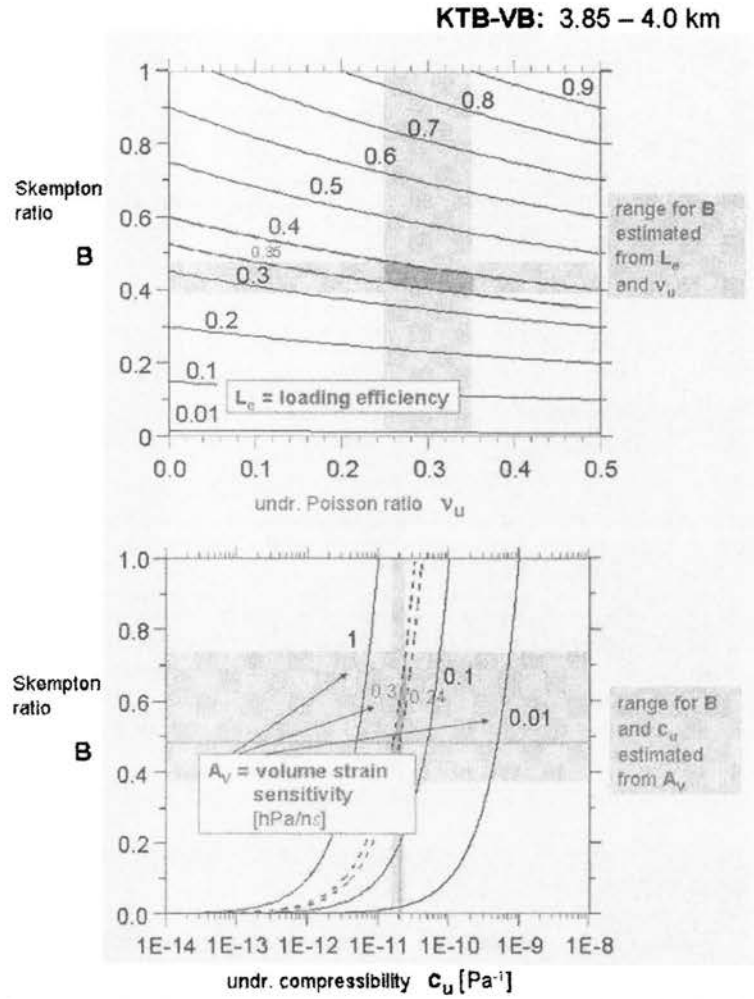

Figure 26: Range of B values compatible with observations of L_e = 1-A_e and realistic estimates for ν_u (top, for H=1); and range of B and c_u values compatible with volume strain sensitivity A_V that depends on both L_e and T_e (bottom; all for well level observations in KTB-VB, cf. see Fig. 25; compiled from [21]).

both in X and Y components except for the lowermost diagram, where the jagged variations are seen in the Y component only. From analysis of much longer time series has been verified that the smooth variations are tidal tilt deformations: The subsurface in the area is inclining in the rhythm of tides due to a superposition of earth tidal forcing and marine tidal loading. As the

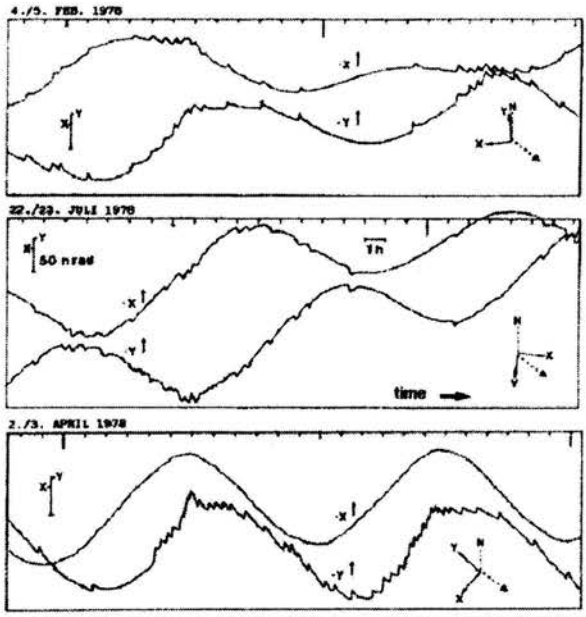

Figure 27: Pump induced tilt signals superimposed on tidal tilt variations at site Medelby, Northern Germany. Recordings are two components (X, Y) of a biaxial tiltmeter at three different instrument orientations with respect to North. The pump causing the jagged tilt anomalies is located 125 m southwest of the tiltmeter (broken line arrows at insets on right). 50 nrad marks on left, based on in-situ calibration of the tiltmeter, scale tilt amplitudes.

ground is water saturated, we have a situation as sketched in the lowermost picture of Fig. 17.

The jagged tilt anomalies result from pumping activities at 125 m distance, reflecting the situation of the second lowermost picture in Fig. 17: A farmer's pump was automatically withdrawing water from ca. 8 m depth whenever a small water tank for the cattle was nearly empty. A first hint on the fact that the farmer's pump caused the anomalies is seen from the way the tilt signals depend on the orientation of the tiltmeter in the borehole: The tilt anomaly vanishes in some azimuth perpendicular to the location of the pump, whereas it appears with similar strength in both signal components when these are roughly oriented 45^o toward the location of the pump (see Fig. 27). The observations of pump induced tilt were made by chance. They became extremely helpful for checking the concept of poroelasticity through further experiments at this site; and have provided additional details of the underlying geophysical processes, as is illustrated below.

Fig. 28 is a map of the test site. The area is rather flat, with grassland

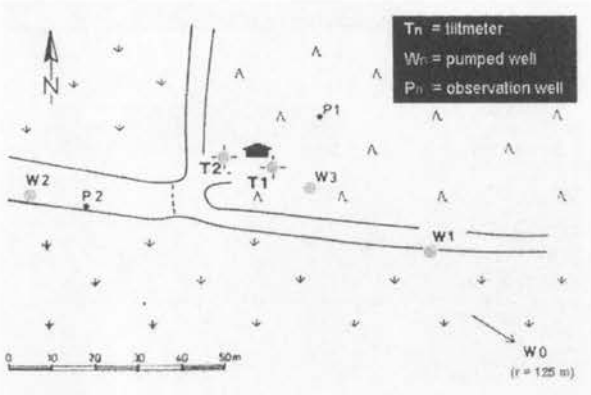

Figure 28: Test site Medelby, Northern Germany, with two tiltmeter boreholes T1, T2, both 30 m deep; three wells W1, W2, W3 for pump tests, 11 m deep (W3: 10 m) with well screens at 8 - 10 m depth (W3: 7 - 9 m); and two wells P1, P2 for additional well level monitoring. The farmer's well causing the tilt anomalies shown in Fig. 27 is W0 (outside the map).

and some woods. The ground water table, depending on the season and the location, varies from about 1.5 to 4 m below surface. Exploratory drilling near well W1 has revealed evidence of a 60 m thick unconfined sandy aquifer of Pleistocene age on top of a massive clay layer. Two tiltmeter boreholes and five wells were drilled at the site for controlled in-situ experiments as the ones that are shown in Figs. 29 to 31. Tilt signals were induced by pumping in wells W1, W2, and W3, respectively (here with observations in T2; similar experiments were done with a tiltmeter in T1). Amplitudes of the induced tilt signals were amazingly large, indicating an excellent coupling of the tiltmeter to the water saturated sands.

Figs. 29 to 31 again demonstrate the dependence of the strike of the induced tilt anomaly from the azimuth of the forcing source. Moreover, pumping and injection appear to produce the same deformation - in opposite direction. The amplitudes of the induced signals scale with the production/injection rates Q for a single well (best seen in Fig. 29), but also seem to depend on the specific geometric configuration of tiltmeter and active well: Fast signal saturation is observed for the configuration T2/W3 (Fig. 31), less rapid saturation for T2/W1 (Fig. 29); no such saturation is seen for T2/W2 (Fig. 30), possibly indicating some non-linear effect here.

The role of the geometric configuration and its influence on the produced

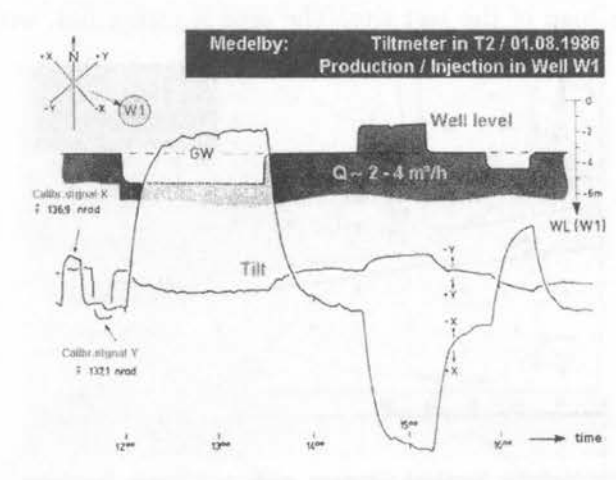

Figure 29: Tilt signals recorded at 30 m depth (lower curves), induced by ground water pumping (two cycles) and injection (one cycle) in well W1 at 53 m horizontal distance at test site Medelby; azimuths of tilt sensors X, Y and direction of well location noted at upper left; tilt amplitudes are scaled by calibration signals at beginning of the test. WL indicates well level depth below top of casing; yield Q was about 4 m/h during first pump cycle and 2 m^3/h during shorter, second one. GW = depth of equilibrium ground water level.

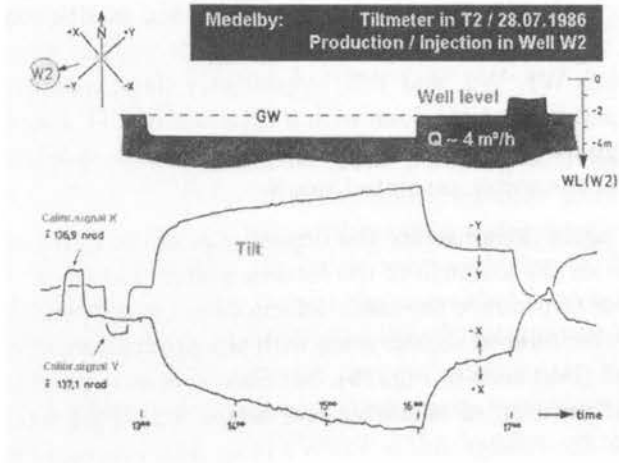

Figure 30: Same as Fig. 29 except for one long cycle of pumping and a short cycle of injection in well W2 at 46 m horizontal distance; Q denotes yield.

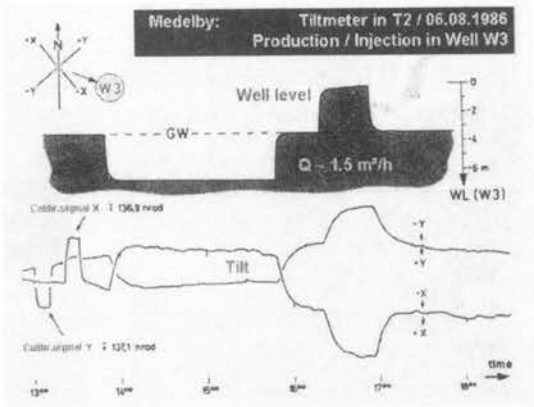

Figure 31: Same as Fig. 29 except for one cycle of pumping and one cycle of injection in well W3 at 21 m horizontal distance; yield Q about 1.5 m/h.

tilt deformation needs a closer look. Fig. 32 displays the situation for the homogeneous full space.

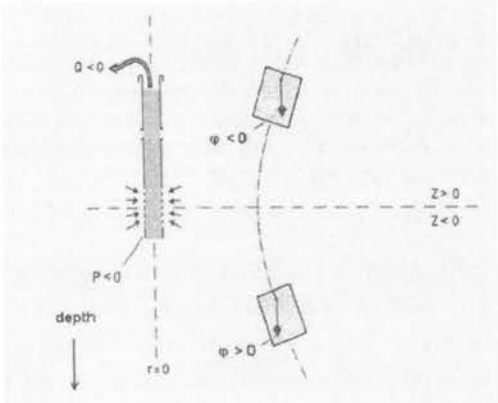

Figure 32: Deformation of an originally vertical subsurface element (curved line) in vicinity of well screen around axis r=0, with production rate Q causing a pore pressure deficit $P < 0$ in homogeneous full space. A tiltmeter (e.g. of type vertical pendulum, as shown) will read a negative tilt φ if placed above the horizontal line z=0 and a positive tilt φ if placed below (sign of tilt as indicated).

As strain-tilt coupling is absent in the full space (no boundary), the tilt is equivalent to shear strain Δ_S. Obviously, tilt is zero on the plane r=0, passing through the centre of a cylindrical source (vertical axis), and on the axis z=0. Assuming a point source for the pumping, strongest shear strains are expected along surfaces of an up-going cone and a down-going cone of

opening angle 45^o, the origins of the cones being the point source. This can well be imagined from Fig. 33. The scheme of the geometric term presented in Fig. 33 will again be referenced when we turn to the half space situation.

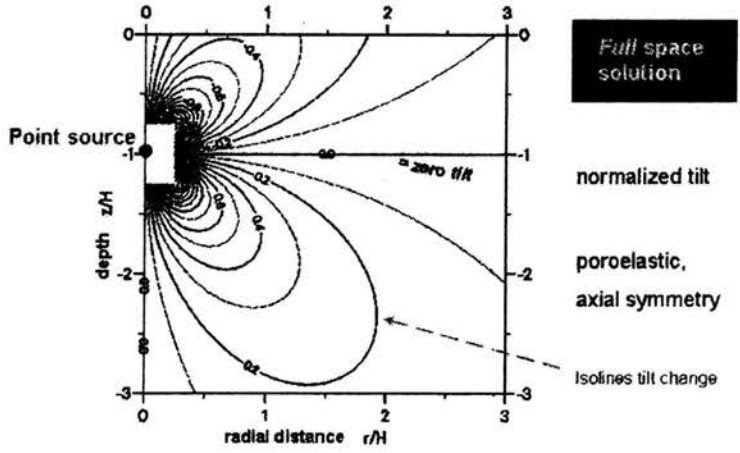

Figure 33: Lines of equal amplitude of geometry term $\varphi^*= [r(z/H+1)]/H/R^{*3}$ characterizing the tilt signal amplitude (= shear strain) in response to pore pressure deficit of type point source at normalized depth -z/H, for normalized radial distances r/H in homogeneous poroelastic full space (after [28]). H here represents the depth below an arbitrary horizontal line z=0; $R^*=[(z/H+1)^2+(r/H)^2]^{-1/2}$.

So far we have assumed that a pump induced tilt deformation is strongest at the azimuth that is pointing toward the forcing well. This certainly will be the case in a homogeneous isotropic medium. Any deviation of the maximum tilt signal by some angle $d\theta$ from the vertical plane spread out by the well's and the tiltmeter's axes (see Fig. 34) would indicate some heterogeneity in the hydro-mechanical behaviour of the subsurface. Such deviation, in fact, has regularly been observed at test site Medelby (Fig. 35).

To verify the presence of heterogeneities in the Pleistocene sands, DC resistivity surveys were carried out at the site. Fig. 36 reveals that occurrence of a zone of enhanced electrical conductivity, possibly reflecting a clay lens, is consistent with a channelling of ground water flow southwest of that zone. Deviations of the pump induced signal from the regular tilt response thus bear information on the subsurface structure. When the induced surface deformation field would be known at sufficiently dense areal coverage, rheological parameters and geometric extension of a

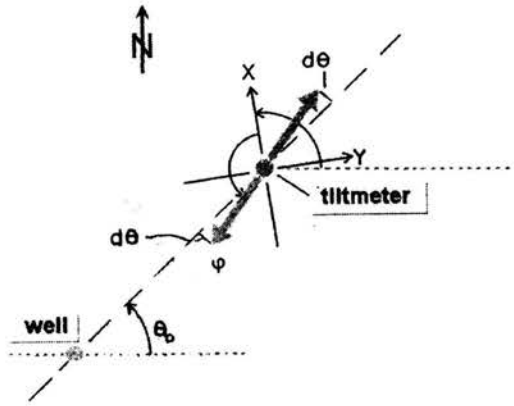

Figure 34: Deviation $d\theta$ of maximum pump induced tilt signal φ from vertical plane that is spread out by axes of the forcing well and of the tiltmeter. θ_o represents arbitrary reference azimuth with respect to North.

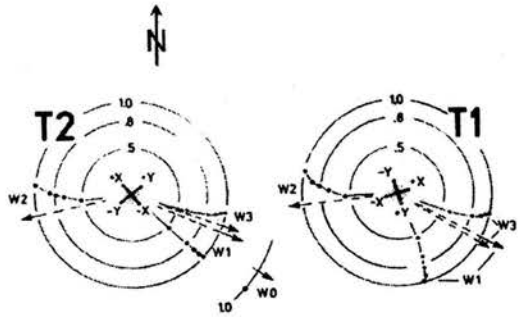

Figure 35: Observation of build-up of pump induced tilt anomalies at tiltmeter locations T1 and T2 at test site Medelby when pumping was initiated in wells W1, W2, W3 (and W0 for T2); see Fig. 28 for locations on map, data from 1986. Arrows indicate directions toward pumping wells; circles denote temporal evolution of induced tilt signals with .5, .8, 1.0 representing 50%, 80% and 100% of approximate total build-up of tilt signal. Angles between arrows and the black points which trace the gradual build-up of the tilt signals mark deviations $d\theta$ as explained in Fig. 34. (Orientations of tiltmeter sensors X, Y as indicated in centres of concentric circles.)

reservoir might be constrained from inversion of the surface observations (see scenario in Fig. 37). For test site Medelby, a fit of the observed signals to the poroelastic full-space solution yields the parameter sets shown in Fig. 38. The value obtained for hydraulic diffusivity D suggests the permeability to be about one order of magnitude lower than is obtained from analysis of conventional hydraulic pump tests.

A quite different example of 'pump'induced tilt is shown in Fig. 39 and

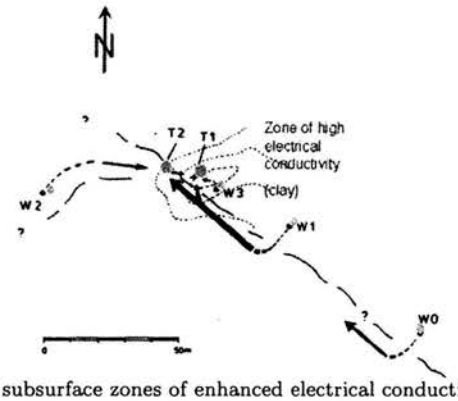

Figure 36: Presence of subsurface zones of enhanced electrical conductivity from DC resistivity survey at site Medelby. Highest conductivity values, possibly reflecting a clay lens, were seen near T1 and W3 (shown isolines are apparent resistivities of 45, 50 and 55 Ohmm, from outer to inner line). Tiltmeters in T1, T2 'see' hydraulic forcings in wells W0 to W3 approaching from directions indicated by arrows (cf. Fig. 35). Preference of tilt signals to occur in northwest - southeast directions (T1 and T2 for pumping in W1 and W2) may indicate preferred flow/enhanced permeability along channel-like structure in this direction.)

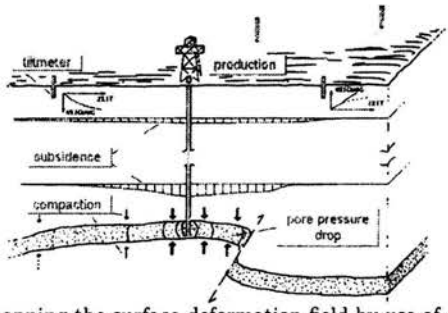

Figure 37: Scenario of mapping the surface deformation field by use of an array of shallow depth tiltmeters to learn about e.g. asymmetric exploitation of a pumped reservoir. For instance, locking of reservoir (right of production hole) could result in more pronounced pore pressure drop, increased compaction, and thus anomalous surface tilt with respect to situation at unlocked side (left of production hole).

Fig. 40. In 1985, an ASKANIA tiltmeter was installed in a borehole on the floor of a gallery in the Grimsel mine, Switzerland (operated by NAGRA). The hole was placed near the entrance of a 150 m long horizontal borehole that was constantly releasing formation water at a yield of 5 liters/min. When its entrance was locked (by a packer), the water pressure steadily rose to almost 4 MPa; when the packer was opened, water flowed out and the pressure immediately dropped to zero. The tiltmeter has recorded the

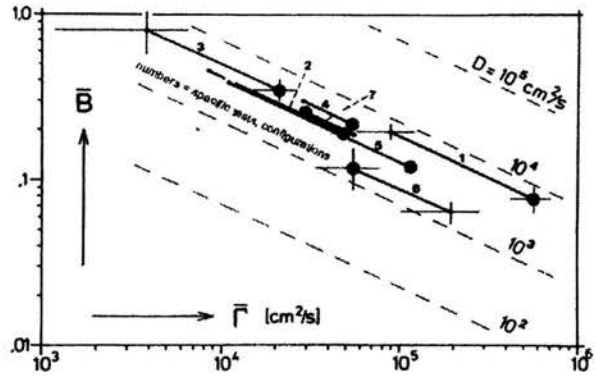

Figure 38: Effective poroelastic parameters consistent with pump induced tilt signals observed at Medelby (cf. Figs. 28-31). Parameters are $\overline{B}=B(1+\nu_u)/[3(1-\nu_u)]$ for vertical axis; $\overline{\Gamma} = \mu(1-\nu_u)(1-\nu)/(\nu_u-\nu)$ for horizontal axis. The tests constrain the in-situ hydraulic diffusivity (= parameter D, broken lines) to values around 4 10^3 cm^2/s.

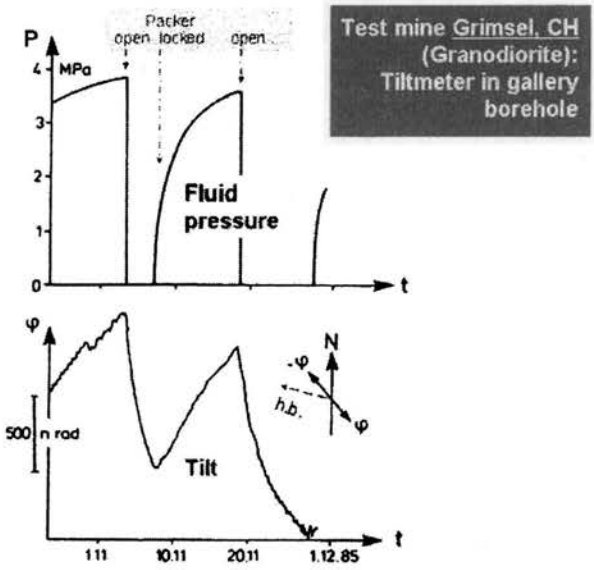

Figure 39: Fluid pressure P in 150 m long horizontal borehole (h.b.) behind packer in test mine Grimsel, Switzerland (top) with tilt φ observed in crystalline rock formation near the packer in direction as shown by inset (bottom); t = time. Large tilt signals resulted from natural hydraulic pressure build-up when the packer was locked, and from pressure release when the packer was opened [29]. Tilt φ was gradually changing although fluid pressure P instantaneously dropped to zero when the packer was opened, indicating the rock deformation to be poroelastic rather than elastic.

amplitude of the pressure induced rock strain to be of order 1 μrad (Fig. 39).

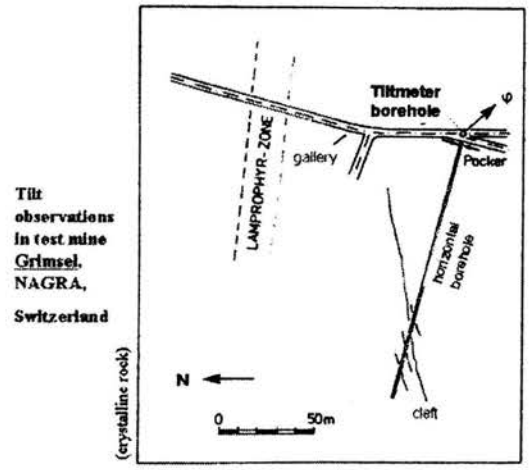

Figure 40: Geometry of the configuration in test mine Grimsel (cf. Fig. 39). The tiltmeter (type ASKANIA vertical pendulum) was operating in 17 m deep borehole below gallery at entrance of packered horizontal borehole. Several prominent clefts were met by the borehole at distance ca. 100 m from its entrance. Deviation of the induced tilt anomaly from direction of the horizontal borehole was probably due to fluid pressure build-up, and release, in these clefts.

Different from the situation in the sands at Medelby, the tilt response due to sudden pressure release (= onset of 'pump test') was much more gradual here, lasting for several weeks rather than for some ten minutes. Permeability of the crystalline granodiorite at Grimsel is roughly six orders of magnitude lower than that of sands. A fit of the tilt response to the poroelastic full space solution suggests the hydraulic diffusivity D to be a factor 10^3 less than at Medelby.

Surprisingly, the maximum tilt signal was clearly not observed in the direction of the horizontal borehole but more towards southeast. The reason, probably, is the influence of a hydraulic pressure build-up not only in the horizontal borehole but also in some clefts that were drilled at ca. 100 m distance from the borehole's entrance (see Fig. 40). Bulk water yield from the clefts was much higher than from the 100 m section of the horizontal borehole southeast of the clefts, suggesting that the clefts are draining a much larger part of the rock than the borehole. They were also found to extend further east and could therefore form an effective source for induced

rock deformation. The clefts do, however, not meet the gallery.

The induced deformations appear to be widely reversible and thus consistent with poroelastic behaviour. The previous example shows that observation of rock deformation can, in principle, be used to detect hidden clefts and fissures when those can be hydraulically loaded. However, the full space scenario that is applicable at Medelby and Grimsel is not valid anymore when tiltmeters are placed at shallow depths.

For tilt observations near the stress-free surface we have to take into account that rotational movements Ω_S become significant. They add to the shear strains $\Delta_S = e_{rz}$ as defined in Fig. 10 and Plate 17 to make up the total vertical tilt $\varphi = \Delta_S + \Omega_S = \frac{1}{2}(\delta u_r \delta z + \delta u_z \delta r) + \frac{1}{2}(\delta u_r \delta z - \delta u_z \delta r) = \delta u_r \delta z$. This superposition completely changes the pattern of pump induced tilt at shallow depths. According to Fig. 33 we would expect a negative tilt above the plane z=0, meaning that the lower part of the tiltmeter body would move closer to the pumping source than its upper part. Instead, as subsidence above the pumped well is one of the consequences of the half space scenario, we will observe that the tiltmeter body in whole inclines toward the well, with its upper part moving closer to the well than its lower part (see Fig. 41).

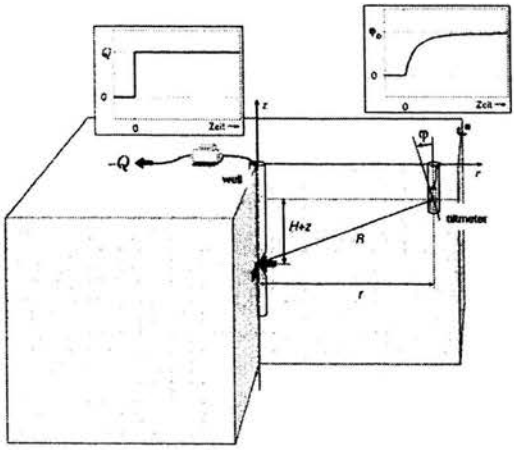

Figure 41: Sketch of tilt response to pumping in nearby well. Note that due to dominance of rotational movements over shear strain, related to surface subsidence above the well, the tiltmeter will record a positive tilt φ rather than a negative as for the full space situation (after [28]).

Only recently the full set of point source solutions for the homogeneous isotropic half space has been presented [28]. These notes will only cite the most striking results. In the half space, plane $z = 0$ (or $z = -H$ in Fig. 33) is no longer the surface with zero tilt. Rather, the surface φ=0 depends on the value of Poisson's ratio ν. Fig. 42 shows that only for ν=0.5 this surface extends to infinity, whereas for $\nu < 0.5$ we obtain a limited zone of tilt $\varphi < 0.5$ around the point source. Tracing the sign of φ along a vertical line within that zone, we find two sign inversions: $\varphi > 0$ at shallow depths, $\varphi < 0$ at medium depths, and again $\varphi > 0$ at greater depths (for $z/H < -1$ near the well).

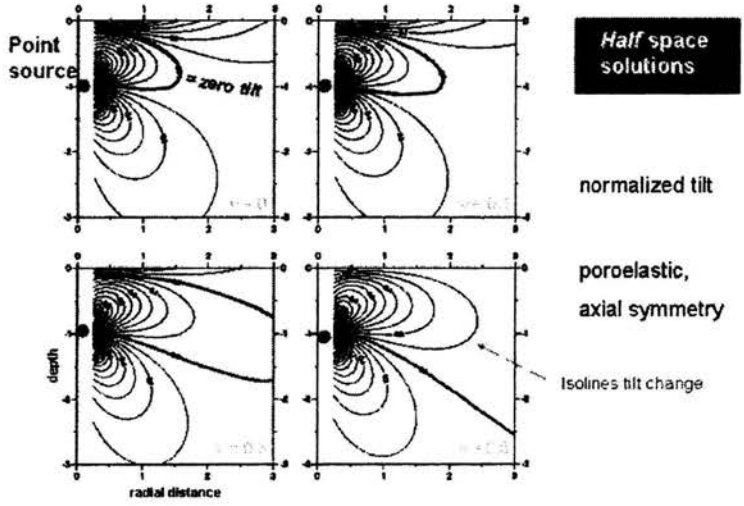

Figure 42: Lines of equal amplitude of geometry term φ^*= [r(z/H+1)]/H/R^{*3} characterizing the tilt signal amplitude (= vertical tilt) in response to pore pressure deficit of type point source at normalized depth -z/H for normalized radial distances r/H in homogeneous poroelastic half space (after [28]). The free surface is at depth zero; R*=[(z/H+1)^2+(r/H)^2]$^{-1/2}$. The surface of zero tilt depends on Poisson's ratio ν, as indicated for four different values of ν (cf. Fig. 33).

Even more recently, a semi-analytical algorithm to forward-model induced deformation within a layered poroelastic medium has been published [30]. By using this algorithm, some pore pressure and induced tilt solutions for multi-layered half spaces are presented in Figs. 43 to 45 (after [31]).

Application of near surface tilt observations for constraining reservoir parameters using the semi-analytical algorithm [30] is shown for a case study. On a patch of land with a groundwater production well near the village of

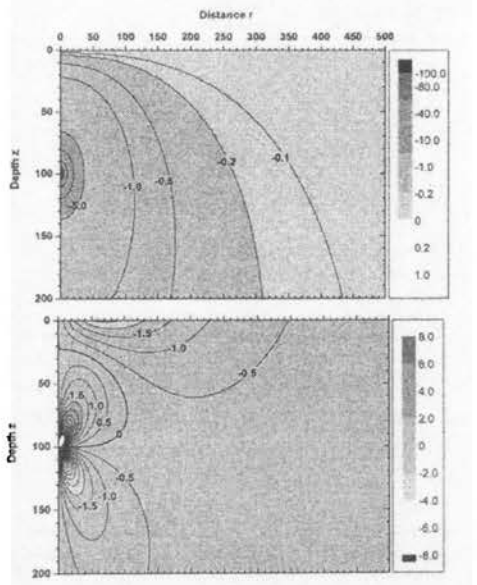

Figure 43: Pore pressure disturbance (top) and induced poroelastic tilt (= -φ , bottom) in half space [31].

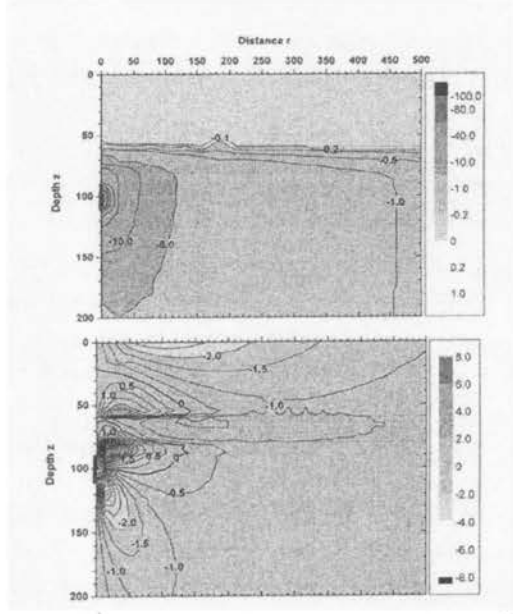

Figure 44: Pore pressure disturbance (top) and induced poroelastic tilt (= -φ , bottom) in three-layer medium [31] (cf. Fig. 43); irregularities are due to grid spacing.

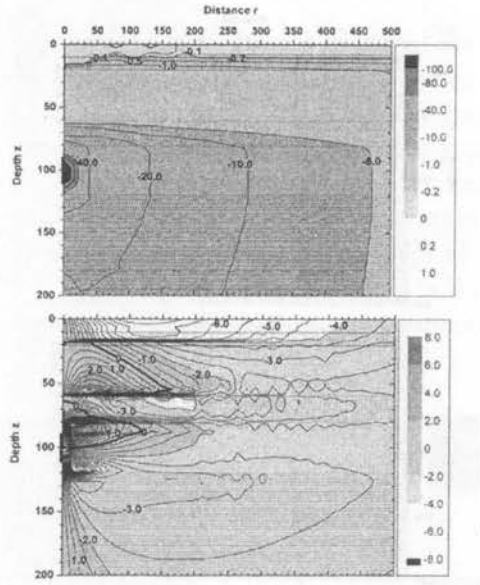

Figure 45: Pore pressure disturbance (top) and induced poroelastic tilt (= $-\varphi$, bottom) in six-layer medium [31] (cf. Fig. 43); irregularities are due to grid spacing.

Nagycenk, Western Hungary, biaxial tiltmeters of type bubble sensor were previously installed at four locations to monitor pump induced deformation at shallow depths [32]. Nominal resolution of the tiltmeters was 0.1 μrad, installation depths were 2 to 4 m, distances from the production well were r_1= 7 m, r_2= 8 m, r_3=23 m, and r_4= 64 m.

Tilt signals induced by pump cycles were clearly seen at all the tiltmeter positions. To first approximation, maximum tilt was observed in the directions pointing toward the production well. Signs of the radial tilt signals were as expected for the half space solution with the top of the tiltmeter body tilting toward the well. Fig. 46 shows a typical recording during week no. 41 in 1996. The pump was active for several hours and was then switched off for aquifer recovery. Amplitude of vertical tilt was ca. 2 μrad at 7 m distance, ca. 4 μrad at 23 m distance. From the driller's notes of the production well was known that the subsurface at the site can be described as an eight layer case of loose sediments (mainly loam, silt, sands and mixtures thereof). The well screen was from 55 m to 72 m depth with a short dead section along an unproductive layer in-between. For forward modelling of the pump induced poroelastic deformation, a set of five grossly estimated parameter values was

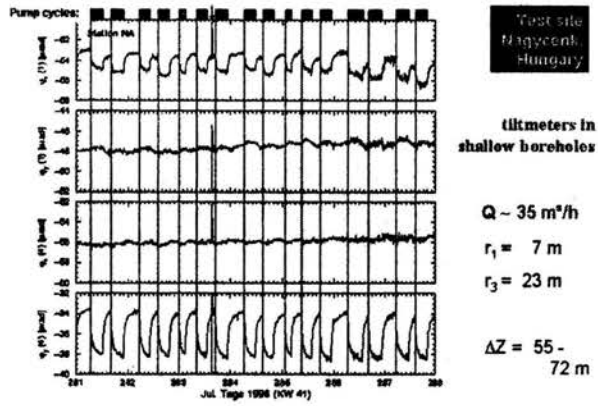

Figure 46: Pump induced tilt signals observed at shallow depths at test site Nagycenk, Hungary. From top to bottom: pump cycles of production well, Q = average yield; radial tilt at distance r_1; tangential tilt at distance r_1; tangential tilt at distance r_3; radial tilt at distance r_3 (radial/tangential tilt means vertical tilt in radial/tangential direction, respectively). ΔZ is the depth range of the productive well screen. Vertical lines mark onsets of pumping. Spike-like tilt distortions at afternoon of day 283 result from passage of teleseismic waves of M_S6.8 earthquake in Cyprus (after [32]).

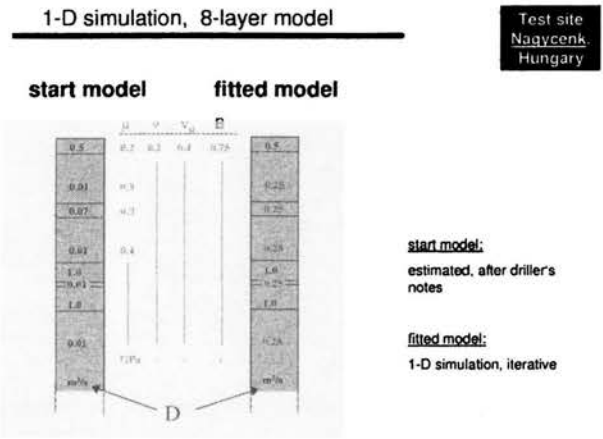

Figure 47: 1-D forward modelling of pump induced tilt in poroelastic 8 layer case. Left: start-ing model; right: fitted model. Parameters of each layer are shear modulus μ, drained and undrained Poisson's ratios ν, ν_u, Skempton ratio B, hydraulic diffusivity D, as indicated. The productive aquifers are layers 5 and 7 (from top) with 1.0 m^2/s hydraulic diffusivity, respectively (top of layer 5 at 55 m depth; bottom of layer 7 at 72 m). Only values for D needed to be adjusted to fit the computational results to observations (after [30]).

attributed to each layer in the start model (Fig. 47).

Fig. 48 has the recordings of the radial tilt components in week no. 42 for distances 7 m and 64 m - together with the respective computed tilts. Although the individual tilt cycles and amplitudes established by the

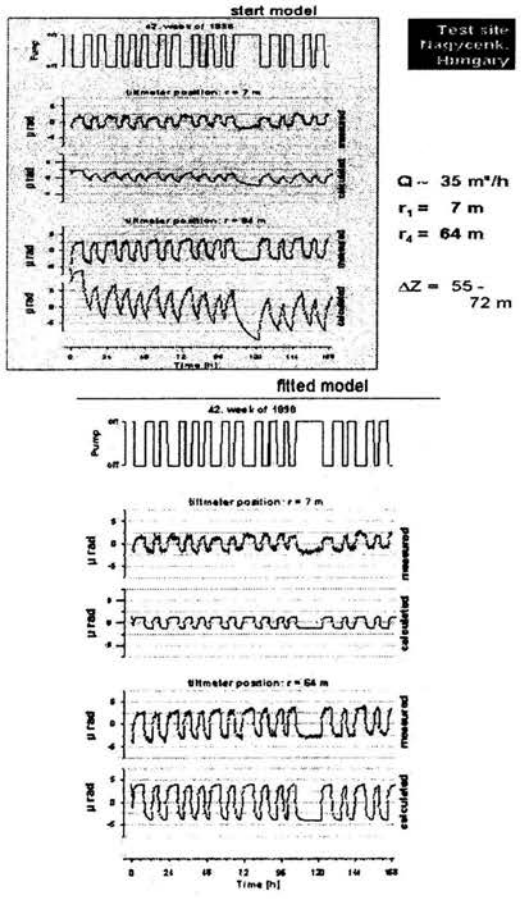

Figure 48: Computed radial tilt response for start model (top) and fitted model (bottom) with observations of radial tilt (more noisy curves) at 7 m and 64 m distances, respectively. Improvement in fitted model is particularly obvious for long pumping cycle from hour 106 to hour 123. Model parameters as in Fig. 47 (after [30]).

start model are approximately reproducing the observations, discrepancies are evident. In particular for a longer pump activity in the week's second half, the observed response is rapidly attaining some stable tilt amplitude,

unlike the computed one.
Through trial and error, parameter values were changed to obtain a better fit. Finally it was found to be sufficient to adjust only the hydraulic diffusivities of the non-productive layers (except for the top layer, the influence of which is of low significance). The D values had to be raised considerably to achieve a satisfactory match. Figs. 48 and 49 demonstrate that the adopted changes lead to improvements at all the distances, from 7 m to 64 m.

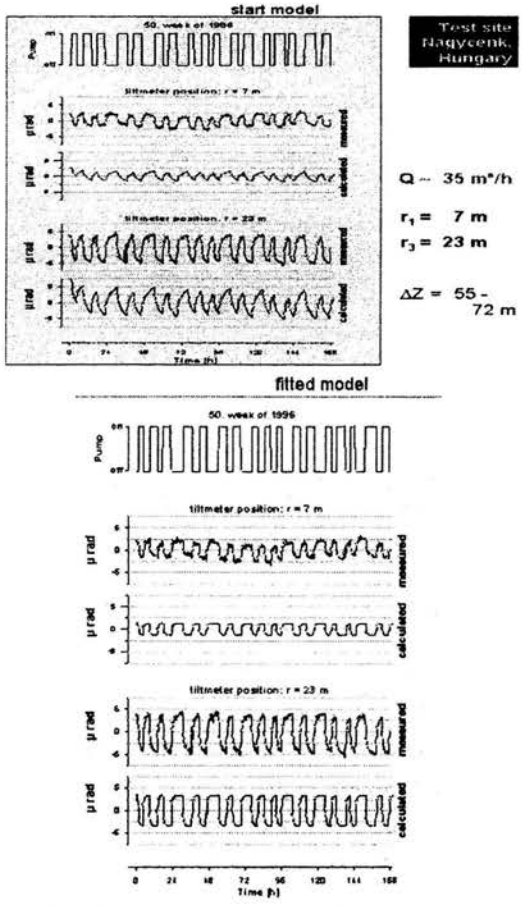

Figure 49: Computed radial tilt response for start model (top) and fitted model (bottom) with observations of radial tilt (more noisy curves) at 7 m and 23 m distances, respectively. Improvement in fitted model achieved for tilt response at 64 m distance also holds for tilt response at 23 m distance. Model parameters as in Fig. 47 (after [30]).

It may be surprising that for the range of radial distances observed at

this site, the tilt response to pumping was steadily increasing with distance. The explanation is the depth of the forcing source in relation to the radial distance. Fig. 42 shows that for realistic values of ν, the largest amplitudes would be expected at distances corresponding to the depth of the well screen. Application of the full space solution would have predicted an inverse sign for the tilt responses.

References

1. KESSELS W., ZOTH K. AND KÜMPEL H.-J., *A pump test where hydrology nearly fails,* Euroconference on Pore Pressure, Scale Effect and the Deformation of Rocks, Abstracts, 16-20 November 1998, Aussois, France, 1998.
2. VERRUIJT, *Elastic storage of aquifers,* In: De Wiest, R.J.M. (ed.), Flow through porous media, Academic Press, New York, pp.331-378, 1969.
3. MARUYAMA T., *Fluid pressure responses of a water-saturated porous elastic multi-layered half-space to water pumping and atmospheric loading,* J. Phys. Earth, Vol.**42**, pp.331-375, 1994.
4. BIOT M.A., *General theory of three-dimensional consolidation,* J. Appl. Physics, Vol.**12**, pp.155-164, 1941.
5. WANG H.F., *Theory of linear poroelasticity with applications to geomechanics and hydrogeology,* Princeton Univ. Press, Princeton, 287p., 2000.
6. KÜMPEL H.-J., *Poroelasticity: Parameters reviewed,* Geophys. J. Int., Vol.**105**, pp.783-799, 1991.
7. NUR AND BYERLEE J.D., *An exact effective stress law for elastic deformation of rock with fluids,* J. Geophys. Res., Vol.**76**, pp.6414-6419, 1971.
8. ZIMMERMAN R.W., SOMERTON W.H. AND KINGM.S., *Compressibility of porous rocks,* J. Geophys. Res., Vol.**91**, pp.12,765-12,777, 1986.
9. SKEMPTON A.W., *The pore -pressure coefficients A and B,* Géotechnique, Vol.**4**, 143-147, 1954.
10. OHKUBO T. AND TERASAKI A., *Physical property and seismic wave velocity of rock* OYO Technical note, TN-22, Tokyo (originally in Soil and Foundation, 19, 1971, in Japanese), 1977.
11. SCHÖN J., *Petrophysik - Physikalische Eigenschaften von Gesteinen und Mineralien,* F. Enke Vlg., Stuttgart, 405p., 1983.
12. RAVALEC M.LE AND GUÉGUEN Y., *High and low frequency elastic moduli for a saturated porous/cracked rock (differential self consistent and poroelastic theories),* Geophysics, Vol. **61**, pp.1080-1094, 1996.
13. RICE J.R. AND CLEARY M.P., *Some basic stress diffusion solutions for fluid-saturated elastic porous media with compressible constituents,* Rev. Geophys. Space Phys., Vol.**14**, pp.227-241, 1976.
14. WANG H.F., *Quasi-static poroelastic parameters in rock and their geophysical applications,* Pure Appl. Geophys., Vol.**141**, pp.269-286, 1993.

15. TERZAGHI K., *Die Berechnung der Durchlässigkeitsziffer des Tones aus dem Verlauf der hydromechanischen Spannungserscheinungen,* Sitzungsber. Akad. Wiss. Wien Math.-Naturwiss. Kl., Abt. 2A, Vol.**132**, p.105, 1923.

16. CLAUSER C., *Permeability of crystalline rocks,* EOS, Transactions, Am. Geophys. Union, Vol.**73**, pp.233+237+238, 1992.

17. INGEBRITSEN ST.E. AND SANFORD W.E., *Groundwater in Geological ProcessesSanford,* Cambridge Univ. Press, Cambridge, 341p., 1998.

18. KÜMPEL H.-J., *Verformungen in der Umgebung von Brunnen,* Habil.thesis (in German), University of Kiel, 198p., 1989.

19. KÜMPEL H.-J., GRECKSCH G., LEHMANN K., REBSCHER D. AND SCHULZE K.C., *Studies of in-situ pore pressure fluctuations at various scales,* Oil & Gas Science and Technology - Rev. IFP, Vol.**54**, pp.679-688, 1999.

20. AGNEW D.C., *Strainmeters and tiltmeters,* Rev. Geophys., Vol.**24**, pp.579-624, 1986.

21. SCHULZE K., KÜMPEL H.-J. AND HUENGES E., *In-situ petrohydraulic parameters from tidal and barometric analyses of fluid level variations in deep wells: Some results from KTB.* - In: Stober, I., and Bucher, K. (eds.), Hydrogeology in Crystalline Rocks, Kluwer Acad. Publ., pp.79-103, 2000.

22. WENZEL H.-G., *Eterna 3.30,* Black Forest Observatory, University of Karlsruhe, 1996.

23. HSIEH P.A., BREDEHOEFT J.D. AND FARR J.M., *Determination of aquifer transmissivity from earth tide analysis,* Water Resour. Res., Vol.**23**, pp.1824-1832, 1987.

24. ROJSTACZER S. AND AGNEW D.C., *The influence of formation material properties on the response of water levels in wells to earth tides and atmospheric loading,* J. Geophys. Res., Vol. **94**, pp.12,403-12,411, 1989.

25. WILHELM H., ZÜRN W., AND WENZEL H.-G., (EDS.), *Tidal Phenomena,* Lecture Notes in Earth Sciences, Vol.**66**, Springer, Heidelberg, 1997.

26. BEAUMONT C. AND BERGER J., *An analysis of tidal strain observations from the United States of America, I, The laterally homogeneous tide,* Bull. Seismol. Soc. Am., Vol.**65**, pp.1613-1629, 1975.

27. BERGER J. AND BEAUMONT C., *An analysis of tidal strain observations from the United States of America: II, The inhomogeneous tide,* Bull. Seismol. Soc. Am, Vol.**66**, pp1821-1846, 1976.

28. LEHMANN K., *Porendruckinduzierte Neigungssignale in geringen Tiefen und ihre Modellierung im homogenen Halbraum,* PhD thesis (in German), Faculty of Mathematics and Natural Sciences, University of Bonn, 185p., Shaker Publ., Aachen, 2001.

29. BGR, *Tätigkeitsbericht 1985/86,* Bundesanstalt für Geowissenschaften und Rohstoffe (BGR), 117p., 1987.

30. WANG R. AND KÜMPEL H.-J., *Poroelasticity - Efficient modelling of strongly coupled, slow deformation processes in multi-layered half-space,* Geophysics, Vol.**68**, pp.705-717, 2003.

31. FABIAN M., ...*www.geo.uni-bonn.de/members/fabian/poromodelle.htm*, 2003.

32. KÜMPEL H.-J., VARGA P., LEHMANN K. AND MENTES GY., *Ground tilt induced by pumping: Preliminary results from the Nagycenk test site, Hungary,* Acta Geod. Geoph. Hung., Vol.**31**, pp.6779, 1996.

33. WAKITA H., *Water wells as possible indicators of tectonic strain,* Science, Vol.**189**, pp.553-555, 1975.

34. ROELOFFS E.A., *Hydrologic precursors to earthquakes: A review,* Pure Appl. Geophys., Vol.**126**, pp.177-209, 1988.

35. KISSIN I.G. AND GRINEVSKY A.O., *Main features of hydrogeodynamic earthquake precursors,* Tectonophysics, Vol.**178**, pp.277-286, 1990.

36. IGARASHI G. AND WAKITA H., *Tidal responses and earthquake-related changes in the water level of deep wells,* J. Geophys. Res., Vol.**96**, pp.4269-4278, 1991.

37. ROELOFFS E.A., *Poroelastic techniques in the study of earthquake-related hydrologic phenomena,* Advances in Geophys., Vol.**37**, pp.135-195, 1996.

38. RUDNICKI J.W., YIN J., J. AND ROELOFFS E.A., *Analysis of water level changes induced by fault creep at Parkfield, California,* J. Geophys. Res., Vol.**98**, pp.8143-8152, 1993.

39. SEGALL P. AND RICE J.R., *Dilatancy, compaction, and slip instability of a fluid-infiltrated fault,* J. Geophys. Res., Vol.**100**, pp.22,155-22,171, 1995.

40. RUDNICKI J.W., *Coupled deformation-diffusion effects in the mechanics of faulting and failure of geomaterials,* Appl. Mechanics Reviews, Vol.**54**, pp.483-502, 2001.

41. GUPTA H.K., *Reservoir-Induced Earthquakes,* Developments in Geotechnical Engineering, 64, Elsevier, Amsterdam, 364p., 1992.

42. GUPTA H.K., RADHAKRISHNA I., CHADHA R.K., KÜMPEL H.-J. AND GRECKSCH G., *Pore pressure studies initiated in area of reservoir induced earthquakes in India,* EOS, Transactions, Am. Geophys. Union, 81/14, April 4, 2000, pp.145+151, 2000.

43. BELL M.L. AND NUR A., *Strength changes due to reservoir-induced pore pressure and stresses and application to Lake Oroville,* J. Geophys. Res., Vol.**83**, pp.4469-4483, 1978.

44. ROELOFFS E.A., *Fault stability changes induced beneath a reservoir with cyclic variations in water level,* J. Geophys. Res., Vol. **93**, pp.2107-2124, 1988.

45. SIMPSON D.W. AND NARASIMHAN T.N., *Inhomogeneities in rock properties and their influence on reservoir induced seismicity,* Gerland's Beitr. Geophys., Vol.**99**, pp.205-219, 1990.

46. GRASSO J.R., *Mechanics of seismic instabilities induced by the recovery of hydrocarbons,* Pure Appl. Geophys., Vol.**139**, pp.506-534, 1992.

47. Shapiro S.A., Rothert E., Rath V. and Rindschwentner J., *Characterization of fluid transport properties of reservoirs using induced microseismicity,* Geophysics, Vol.**67**, pp.212-220, 2002.

48. Okada Y., *Internal deformation due to shear and tensile faults in a half-space,* Bull. Seis. Soc. Am., Vol.**82**, pp.1018-1040, 1992.

49. Grecksch G., Roth F. and Kümpel H.-J., *Coseismic well level changes due to the 1992 Roermond earthquake compared to static deformation of half-space solutions,* Geophys. J. Int., Vol.**138**, pp.470-478, 1999.